Effect of pre-corroded on fatigue behavior of MAO treated ZK60 magnesium alloy in a simulated body fluid

Ying Xiong[1, 2*)], Jie Yang[1)], Yi Yu[1)], Liuyong He[1)]

1) College of Mechanical Engineering, Zhejiang University of Technology, Hangzhou 310023, China
2) Key Laboratory of Special Purpose Equipment and Advanced Processing Technology, Ministry of Education and Zhejiang Province, Zhejiang University of Technology, Hangzhou 310023, China

E-Mail: yxiong@zjut.edu.cn
*To whom correspondence should be addressed.

ABSTRACT

A bio-ceramic coating was prepared on the surface of ZK60 magnesium alloys by micro-arc oxidation (MAO) method. The substrate (BM) and coated (MAO) specimens were pre-corroded in a simulated body fluid (SBF) for 12 h. Strain-controlled and stress-controlled loading modes were used to conduct fatigue tests for the two specimens, respectively. The cyclic deformation behavior of the two specimens with non-corroded and pre-corroded was studied. The mechanism of cyclic deformation under different loading conditions is related to twinning and slip. At the same test conditions, the fatigue life of the non-corroded BM specimen is higher than that of the non-corroded MAO specimen, while the fatigue life of the pre-corroded MAO specimen is higher than that of the pre-corroded BM specimen. A modified total strain energy model is proposed and the precision of life prediction is higher than that of traditional fatigue model.

Keywords: Magnesium alloys; cyclic deformation; MAO coating; Simulated body fluid; Fatigue life prediction

1. Introduction

At present, magnesium alloys as degradable implant materials have attracted wide attention in the medical field. Different from traditional implant materials (titanium alloy, stainless steel and cobalt-chromium alloy, etc.), the temporary implants made of magnesium alloy can be gradually degraded in physiological environment, and thus avoiding the damage caused by secondary surgery [1-3]. In addition, the density and elastic modulus of magnesium alloy implants are close to human bone, which can effectively avoid stress shielding effect [4,5]. However, the poor corrosion resistance of magnesium alloys makes it easy to degrade rapidly in physiological environment, which limits its clinical application as a biological implant [6-8].

MAO technology has been used to prepare bio-ceramic coatings on the surface of magnesium alloys to improve the corrosion resistance and bioactivity of materials [9-15]. Magnesium alloy implants must have sufficient resistance to stress corrosion cracking (SCC) under both corrosive body fluids and mechanical loads in human environment. The stress corrosion behavior of MAO coated magnesium alloys in SBF is reported. Xiong et al [16, 17] conducted a slow strain rate tensile test (SSRT) for untreated and MAO treated AZ80 magnesium alloys in SBF, and the results indicated that the stress corrosion resistance of MAO treated magnesium alloys is higher than that of untreated

magnesium alloy. A composite MAO coating is prepared on the surface of Mg-4Zn-0.6Zr-0.4Sr magnesium alloy by Chen et al [18]. The results of SSRT tests combined with in-situ electrochemical measurements showed that the SCC resistance of MAO coated magnesium alloy in the SBF is significantly improved. However, medical implants often bear cyclic loads in human environment, which can lead to sudden rupture of implants before completing their functions. Sudden failure of implants can have serious consequences, such as causing pain or inflammation in surrounding tissues [19]. Therefore, medical magnesium alloy implants must have mechanical integrity. Jafari et al. [20] investigated the fatigue behavior of AZ91D magnesium alloys in modified simulated body fluid (m-SBF). The results showed that the crack initiation occurs at inclusions and corrosion pits, and the hydrogen embrittlement plays an important role in crack propagation in m-SBF. Liu et al. [21] investigated the fatigue behavior of extruded Mg–Zn–Y–Nd alloy used for vascular stents was studied both in air and in SBF. The results showed that the fatigue limit of the alloy is about 65 MPa at 10^7 cycles in air, while there is no limit in SBF. The stress corrosion and hydrogen embrittlement were the main reasons for inducing fatigue crack initiation in magnesium alloys in SBF. Chen et al. [22] studied ratcheting and fatigue behaviors of extruded AZ31B magnesium alloys in phosphate buffered solution (PBS). The results showed that the interaction between corrosion and ratcheting strain leads to fatigue damage of magnesium alloy. Severe corrosion environments and larger ratcheting strains induce more micro-cracks on the surface of material, which accelerated the fatigue damage process. Although some researchers have investigated the fatigue behavior of magnesium alloys in SBF, the study on fatigue behavior of MAO treated magnesium alloys in SBF has not been reported.

In this paper, a bio-ceramic coating was prepared on the surface of ZK60 magnesium alloys by using MAO method. The fatigue tests were carried out by strain-controlled and stress-controlled loading, respectively. The cyclic deformation behavior of substrate (BM) and coated (MAO) specimens with non-corroded and pre-corroded was studied. The total strain energy model was used to predict the fatigue life of various specimens under different loading conditions.

2. Materials and methods

The test material is an extruded ZK60 magnesium alloy. The long axis of the plate specimen for fatigue test is parallel to the extrusion direction, and the dimension of the gauge segment is 4 mm (thickness) × 4.5mm (width) × 8 mm (length). Before preparing the MAO coating, all the specimens were polished by using SiC papers with grit No. from 400 up to 1200, and ultrasonically washed in anhydrous ethanol, then cleaned with distilled water and dried in ambient air. The composition of electrolyte and the electrical parameters used to prepare MAO coating was published in previous paper [23]. The SBF solution [12] is composed of 6.8 g/L NaCl, 0.1 g/L Mg_2SO_4, 0.2 g/L $CaCl_2$, 2.2 g/L $NaHCO_3$, 0.216 g/L NaH_2PO_4, 0.026 g/L Na2HPO4, 0.4 g/L KCl. The pH value of SBF solution is 7.4, which was regulated by NaOH solution and dilute HCl solution. For all the specimens, the part except the gauge section were wrapped with anticorrosive tape to avoid corrosion, and then immersed in the SBF for 12 h. The pre-corroded specimens were dried in ambient air and the adhesive tape was removed.

Fatigue experiments were conducted in ambient air using Instron8872 servo-hydraulic material testing systems. The non-corroded and pre-corroded (BM and MAO) specimens were subjected to cyclic loading tests under the strain-controlled and stress-controlled loading, respectively. The fully reversed strain-controlled tests were conducted with the strain amplitudes between 0.5% and 1.0%.

Three stress amplitudes (150 MPa,180 MPa and 200 MPa) and three stress ratios (–0.5, –0.8 and –1) were used in the stress-controlled experiments. The fatigue test conditions are listed in Table 1 and 2, respectively.

Table 1
Strain-controlled fatigue tests

Spec ID	Environment	$\Delta\varepsilon/2$ (%)	f (Hz)	R_ε	N_f (Cycle)
60-BM-A1	non-corroded	1	0.33	-1	376
60-BM-A2	non-corroded	0.8	0.33	-1	491
60-BM-A3	non-corroded	0.7	0.33	-1	510
60-BM-A4	non-corroded	0.5	1	-1	2942
60-BM-A5	pre-corroded	1	0.33	-1	193
60-BM-A6	pre-corroded	0.8	0.33	-1	292
60-BM-A7	pre-corroded	0.7	0.33	-1	351
60-BM-A8	pre-corroded	0.5	1	-1	240
60-MAO-A1	non-corroded	1	0.33	-1	308
60-MAO-A2	non-corroded	0.8	0.33	-1	460
60-MAO-A3	non-corroded	0.7	0.33	-1	385
60-MAO-A4	non-corroded	0.5	1	-1	199
60-MAO-A5	pre-corroded	1	0.33	-1	256
60-MAO-A6	pre-corroded	0.8	0.33	-1	402
60-MAO-A7	pre-corroded	0.7	0.33	-1	360
60-MAO-A8	pre-corroded	0.5	1	-1	135

$\Delta\varepsilon/2$= strain amplitude; f= frequency;R_ε= strain ratio; N_f= number of cycles to failure.

Table 2
Stress-controlled fatigue tests

Spec ID	Environment	$\Delta\sigma/2$ (MPa)	f (Hz)	R_σ	σ_m (MPa)	N_f (Cycle)
60-BM-R1	non-corroded	200	0.5	-0.5	67	2146
60-MAO-R1	non-corroded	200	0.5	-0.5	67	1379
60-BM-R3	pre-corroded	200	0.5	-0.5	67	1202
60-MAO-R3	pre-corroded	200	0.5	-	67	1356

				0.5		
60-BM-R5	non-corroded	180	1	-1	0	644
60-MAO-R5	non-corroded	180	1	-1	0	414
60-BM-R6	pre-corroded	180	1	-1	0	344
60-MAO-R6	pre-corroded	180	1	-1	0	385
60-BM-R7	non-corroded	180	1	-0.8	20	778
60-MAO-R7	non-corroded	180	1	-0.8	20	724
60-BM-R8	pre-corroded	180	1	-0.8	20	338
60-MAO-R8	pre-corroded	180	1	-0.8	20	396
60-BM-R9	non-corroded	200	0.5	-0.8	23	382
60-MAO-R9	non-corroded	200	0.5	-0.8	23	317
60-BM-R11	pre-corroded	200	0.5	-0.8	23	188
60-MAO-R11	pre-corroded	200	0.5	-0.8	23	244
60-MAO-R14	non-corroded	180	1	-0.5	60	2265
60-MAO-R15	pre-corroded	180	1	-0.5	60	2208
60-MAO-R16	non-corroded	150	3	-0.5	50	6687
60-MAO-R17	pre-corroded	150	3	-0.5	50	5777
60-MAO-R18	non-corroded	150	3	-1	0	10222
60-MAO-R19	pre-corroded	150	3	-1	0	6397

$\Delta\sigma/2 = stress\ amplitude$; f=frequency; R_σ=¿stress ratio; σ_m=mean stress;

N_f = number of cycles to failure.

3. Results

3.1. Tensile properties

Tensile stress-strain curves of the non-corroded and pre-corroded (BM and MAO) specimens are shown in Fig. 1. Taking 0.2% offset as a measure of the yield stress, the tension yield stresses/ elongation of non-corroded BM and non-corroded MAO specimens are 286 MPa/27.6% and 283 MPa/26.7%, whereas pre-corroded BM and pre-corroded MAO specimens are 275 MPa/20.5% and

279 MPa/21.5% respectively. It can be seen that the tensile yield strength of the pre-corroded BM and pre-corroded MAO specimens decreased by 4% and 1.4% compared with the non-corroded BM and non-corroded MAO specimens, respectively. The previous research reveals that the compressive yield stress of ZK60 magnesium alloy is 159 MPa [24]. The Chen et al [26] pointed out that the degree of reduction of compressive yield strength is similar to that of the tensile yield strength in the corrosion environment for the magnesium alloys.

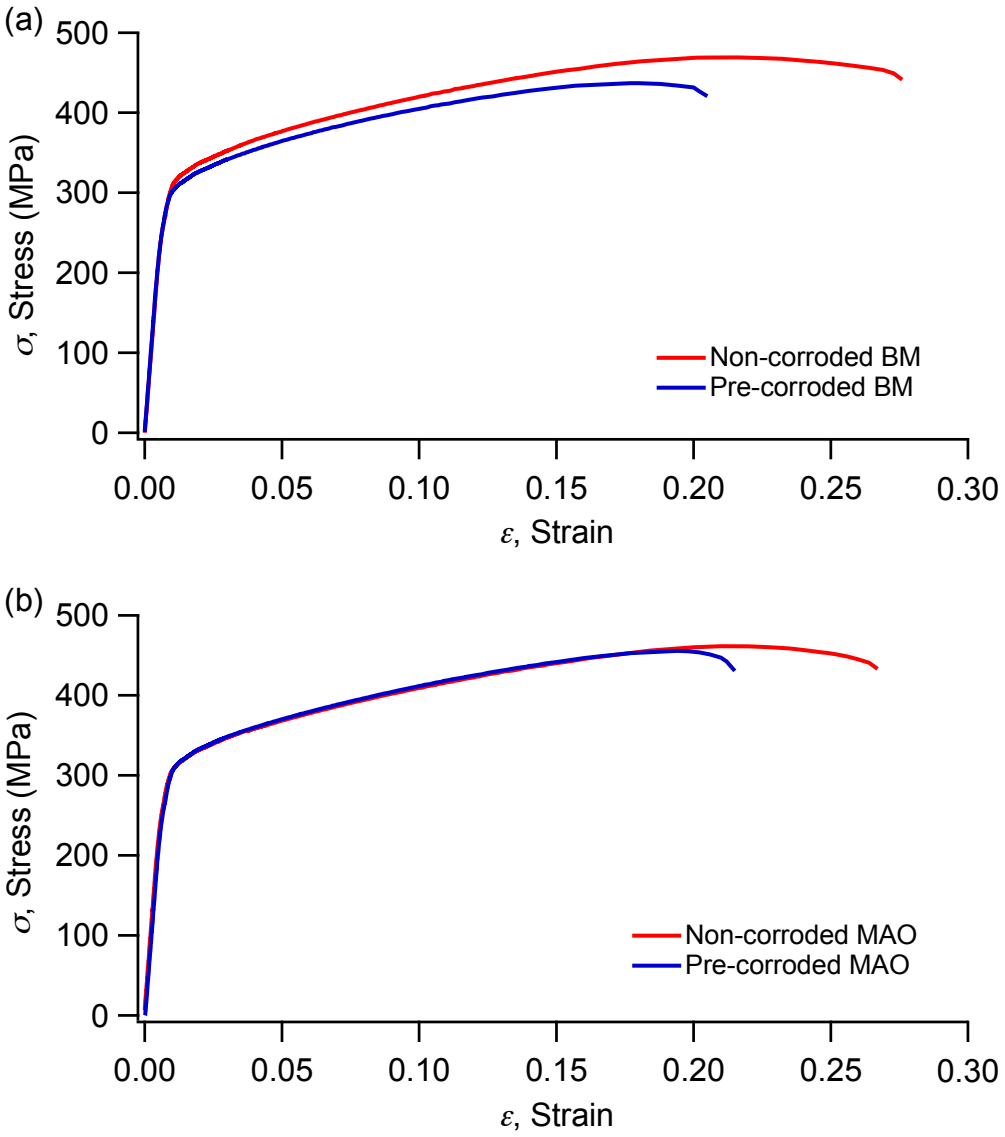

Fig. 1. Tensile stress-strain curves of ZK60 magnesium alloy for different specimens.

3.2. Cyclic deformation behavior at strain-controlled loading

The stress-strain hysteresis loops of all the specimens (BM and MAO) with non-corroded and pre-corroded under full reversed strain-controlled loading are shown in Fig. 2. For each experiment, the stress-strain hysteresis loops are shown for the 20th loading cycles, the loading cycles approximately corresponding to a quarter, a half and three quarter of fatigue life. For the non-corroded (BM and MAO) specimens (Fig. 2a and c), the hysteresis loops indicate an asymmetric shape during the whole cyclic loading at the strain amplitude between 0.7% and 1.0%. Compression

reversal is a concave-up shape caused by the formation of tension twinning, while tension reversal is a sigmoidal shape composed of a concave-down shape dominated by detwinning and a concave-up shape dominated by non-base slip [25]. This type of twinning-detwinning deformation was named as "partial twinning-detwinning" [24]. When the strain amplitude is reduced to 0.5%, the maximum tensile stress (224 MPa) and the maximum compressive stress (153 MPa) in the BM specimen during each cyclic loading are lower than the monotonic tensile yield stress (286 MPa) and the monotonic compressive yield stress (159 MPa), respectively. The hysteresis loops of the two specimens (BM and MAO) show a tension-compression symmetric during the cyclic loading. This means that twinning and detwinning are not involved in the compression and tension reversal, and dislocation slip dominated cyclic deformation [25]. However, the hysteresis loops of the pre-corroded (BM and MAO) specimens (Fig. 2b and d) show an asymmetric shape at the strain amplitude between 0.5% and 1.0%. The compression reversal only exhibits a concave-up shape and the tension reversal indicates a sigmoidal shape. It shows that partial twinning-detwinning dominate cyclic deformation at the strain amplitudes ranging from 0.5% to 1.0%.

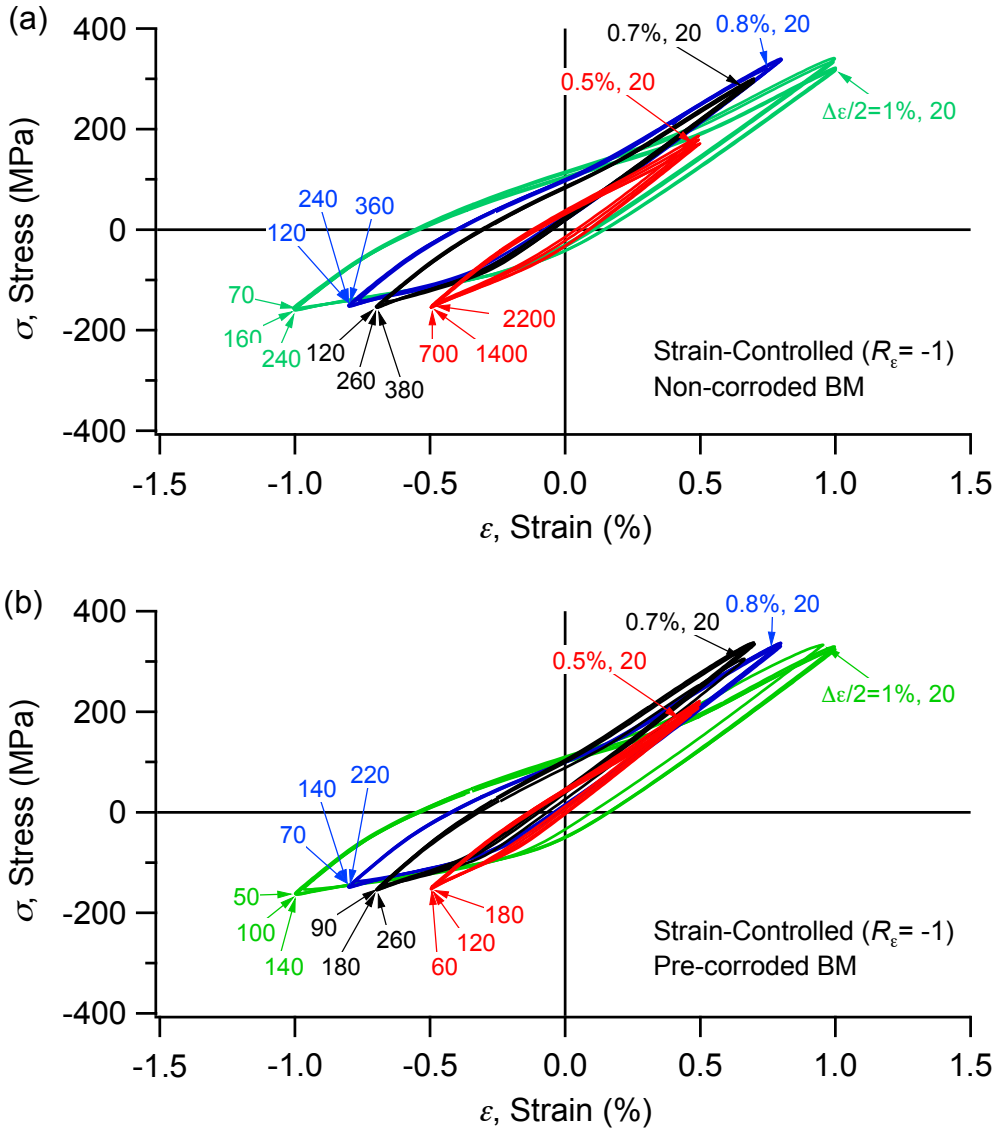

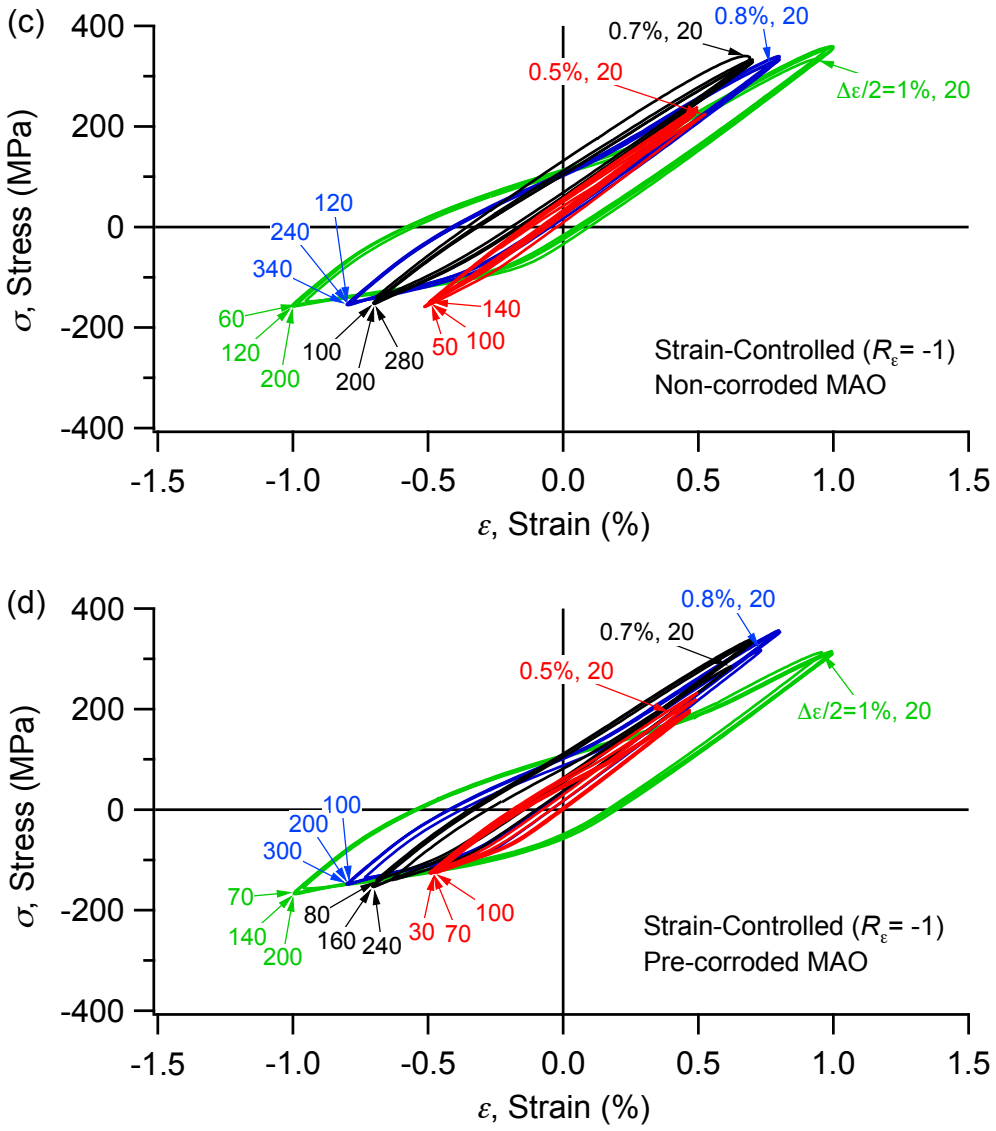

Fig.2. Cyclic stress-strain hysteresis loops under fully reversed strain-controlled loadings: (a) non-corroded BM specimens; (b) pre-corroded BM specimens; (c) non-corroded MAO specimens and (d) pre-corroded MAO specimens.

Fig. 3 shows the evolutions of the stress amplitude with the cycle numbers under different strain amplitudes. When the strain amplitude ranges from 0.7% to 1%, the stress amplitudes of non-corroded and pre-corroded (BM and MAO) specimens increase with the increase of loading cycles, showing a cyclic hardening behavior. When the strain amplitude decreases to 0.5%, the stress amplitude of the non-corroded BM specimen almost keeps a value during the loading cycles, meaning that there is no obvious cyclic hardening and cyclic softening, however, the stress amplitude of the non-corroded MAO specimen increases with the cycle number increasing, exhibit a cyclic hardening (Fig. 3a). At the each strain amplitudes, the stress amplitudes of pre-corroded (BM and MAO) specimens increase with the increase of cycle numbers, showing cyclic hardening (Fig. 3b).

For the non-corroded specimen (Fig. 3a), the stress amplitude of MAO specimens is larger than that of BM specimens at the same strain amplitude. This means that MAO specimens are more prone to fatigue failure compare with BM specimens, that is, MAO treatment can not improve the fatigue

life of materials in the air environment. Due to defects such as micro-pores and micro-cracks on the surface of the MAO coating, fatigue cracks are easy to initiate at the defects during cyclic loading [27, 28].

For pre-corroded specimens (Fig. 3b), when the strain amplitude is higher than 0.7%, the stress amplitude of the MAO specimen is lower than that of the BM specimen, and the fatigue life of the former is higher than that of the latter at the same strain amplitude. This indicates that the MAO coating plays a protective role on the substrate in the corrosion environment at the higher strain amplitudes, and thus improving the corrosion fatigue resistance of the substrate. When the strain amplitude decreases to 0.5%, however, the stress amplitude of the MAO specimen is greater than that of the BM specimen, and the fatigue life of the latter is higher than that of the former (Fig. 3b). This shows that the anti-corrosion fatigue effect of MAO coating is only reflected in the higher strain amplitude.

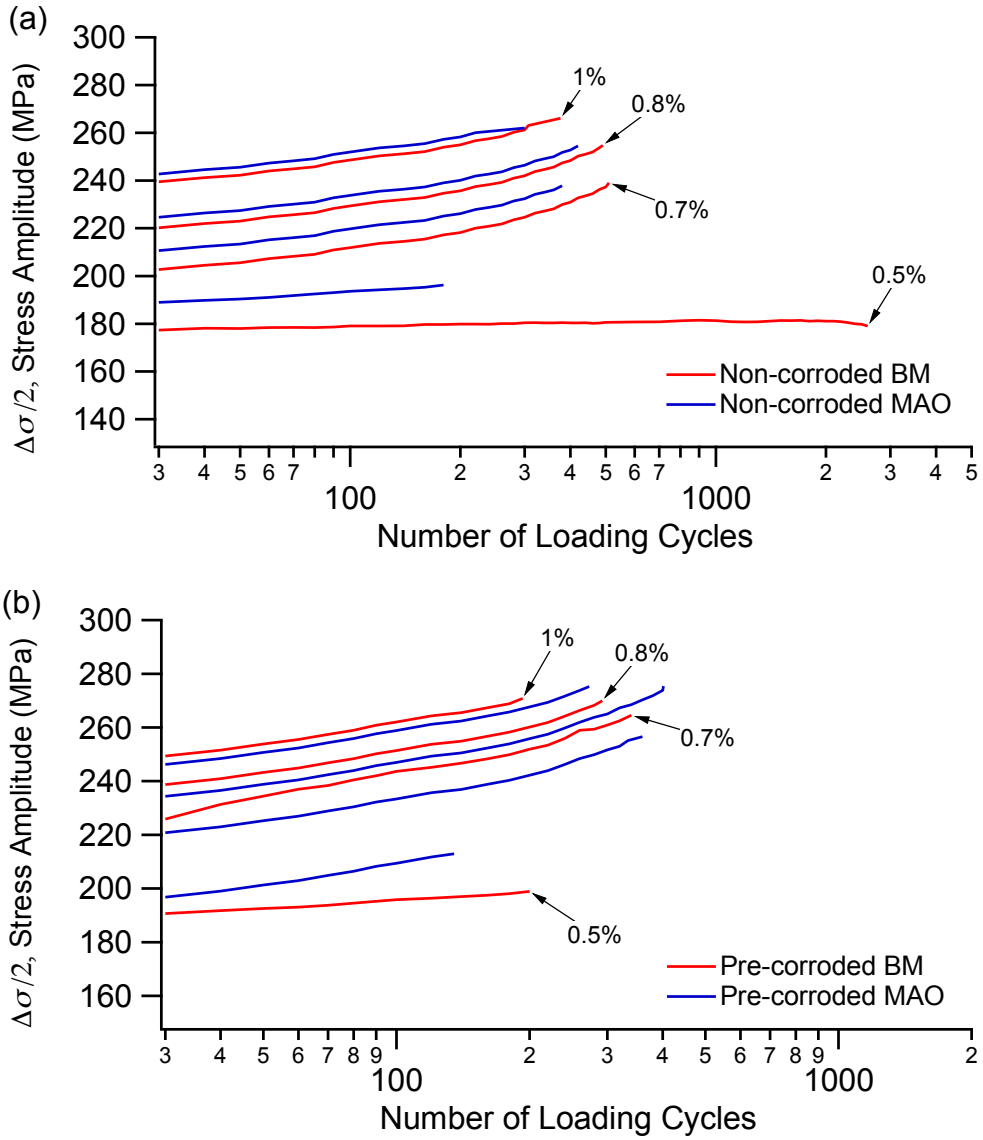

Fig. 3. Evolutions of stress amplitude with cycle numbers under fully reversed strain-controlled loadings: (a) non-corroded specimens and (b) pre-corroded specimens.

3.2. Cyclic deformation behavior at stress-controlled loading

3.3.1 Stress ratio of $R_\sigma = -0.5$

At the stress ratio of –0.5, the shape and evolution of the hysteresis loops of BM specimens are similar to that of MAO specimens at the same stress amplitude. Fig. 4 shows the evolution of the hysteresis loops in the MAO specimens at the different stress amplitudes. When the stress amplitude is 200 MPa (Fig. 4a and b), the cyclic stress range is between 267 MPa (maximum stress) and -133 MPa (minimum stress). The maximum tensile stress and maximum compressive stress are lower than the tensile yield and compressive tensile yield stress, respectively. It means that tension twinning is difficult to be activated during cyclic loading. However, the stress-controlled mode causes large deformation of the material at the initial stage of loading, which leads to the activation of tension twinning in some favorable oriented grains [24]. Therefore, the hysteresis loops of the non-corroded (Fig. 4a) and pre-corroded (Fig. 4b) specimens at the first 40 cycles show obvious asymmetric shape. The asymmetric hysteresis loops indicate that twinning-detwinning dominate cyclic deformation of material. As the loading cycles increase, the shape of the hysteretic loops gradually changes from asymmetry to symmetry, which means that the cyclic deformation mechanism changes from twinnig-detwinnig to dislocation slip. This is because the twinned grains are difficult to re-twinning after they are detwined. As the number of cycle increases, the re-twinning requires a higher compressive stress to be activated [29]. Therefore, the cyclic deformation mechanism after the initial stage until the fatigue failure is dislocation slip. In addition, with the increase of loading cycle, the minimum strain, ϵ_{min} and the maximum strain, $\epsilon_{max}$of the specimens in both environments moves in a positive direction. During the whole cyclic loading process, the minimum strain of the non-corroded MAO specimen decreased by about 0.5%, while the pre-corroded MAO specimen decreased by about 0.35%.

At the stress amplitudes of 180 MPa (Fig. 4c and d) and 150 MPa (Fig. 4e and f), the shape of hysteresis loops of the MAO specimens in the different environments remain symmetrical during the cyclic loading. With the decrease of stress amplitude, the size of the hysteretic loops decreases and the symmetry is more obvious. In this case, dislocation slip dominates the cyclic deformation, the ϵ_{max} andϵ_{min} simultaneously moves in a positive direction as the loading cycles increases.

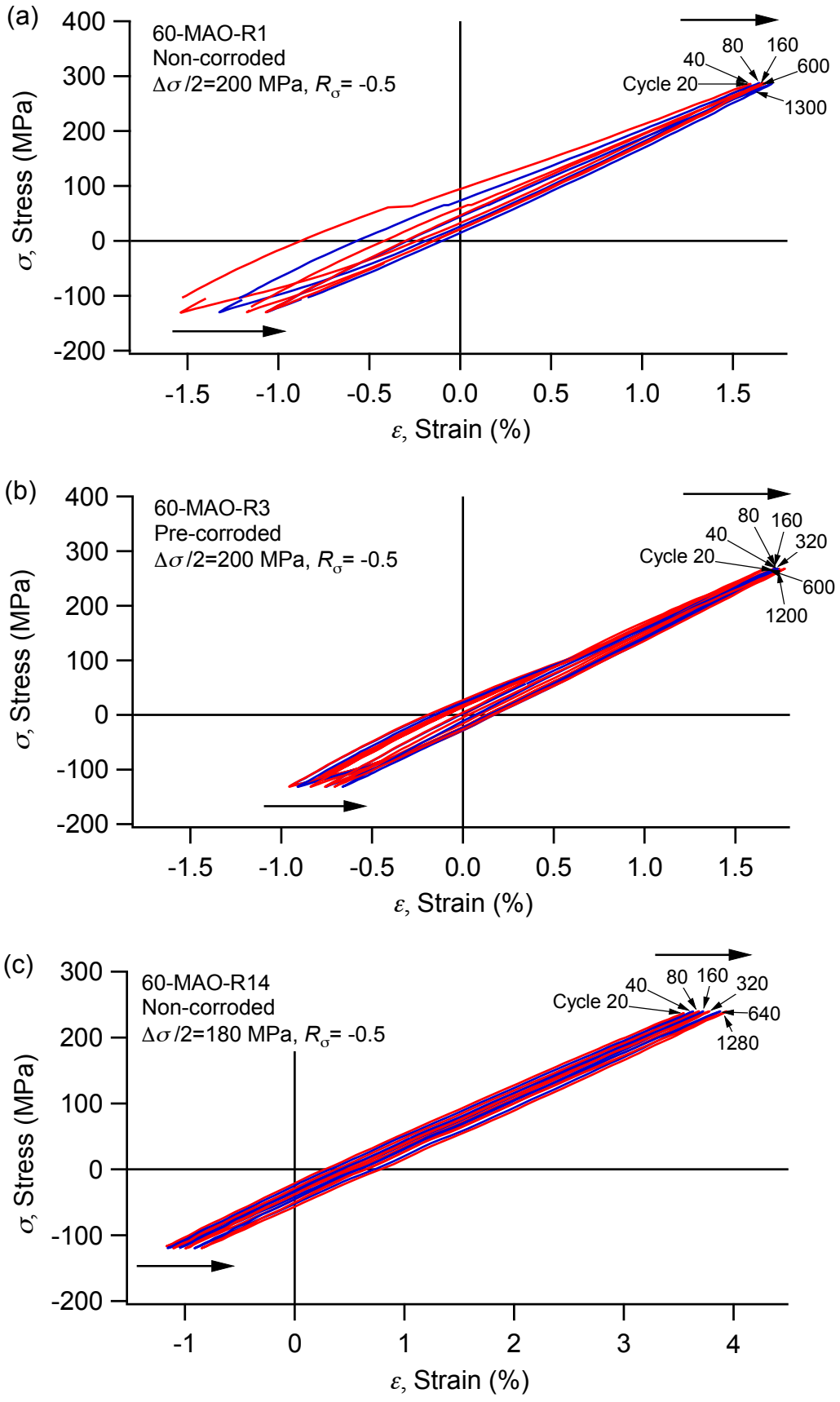
(a)
60-MAO-R1
Non-corroded
Δσ/2=200 MPa, Rσ= -0.5
Cycle 20
40
80
160
600
1300
σ, Stress (MPa)
ε, Strain (%)
(b)
60-MAO-R3
Pre-corroded
Δσ/2=200 MPa, Rσ= -0.5
Cycle 20
40
80
160
320
600
1200
σ, Stress (MPa)
ε, Strain (%)
(c)
60-MAO-R14
Non-corroded
Δσ/2=180 MPa, Rσ= -0.5
Cycle 20
40
80
160
320
640
1280
σ, Stress (MPa)
ε, Strain (%)

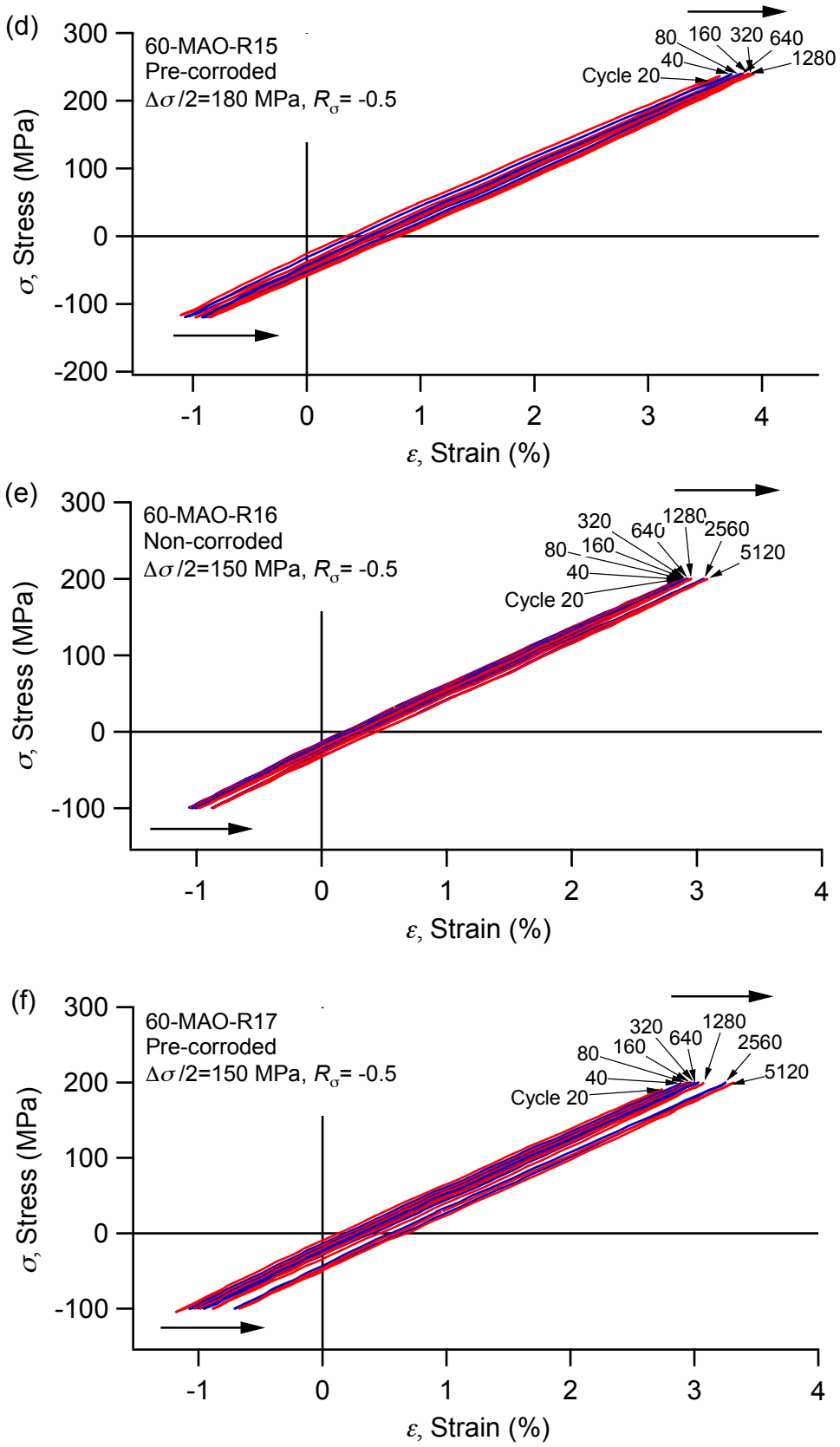

Fig. 4. Cyclic stress-strain hysteresis loops of MAO specimens at stress ratio of –0.5: a) $\Delta\sigma/2$ = 200 Mpa, non-corroded; b) $\Delta\sigma/2$ = 200 Mpa, pre-corroded; c) $\Delta\sigma/2$ = 180 Mpa, non-corroded; d) $\Delta\sigma/2$ = 180 Mpa, pre-corroded; e) $\Delta\sigma/2$ = 150 Mpa, not-corroded; f) $\Delta\sigma/2$ = 150 Mpa, pre-corroded.

Ratcheting strain is conventionally defined as the mean strain, ϵ_m, which is the average value of the maximum strain, ϵ_{max}, and the minimum strain, ϵ_{min}, in a loading cycle under uniaxial loading [24]. Fig. 5 shows the evolutions of ratcheting strain with the cycle numbers for all the specimens under the different stress amplitude with stress ratio of –0.5. When the stress amplitude is 200 MPa (Fig. 5a), the not-corroded (BM and MAO) specimens show a compressive ratcheting strain during the whole cyclic loading. The ratcheting strain decreases with the cycle number increasing at the initial loading stage. The stress-strain hysteresis loops in this period are asymmetric (Fig. 4a), and twinning-detwinning dominate the cyclic deformation in the initial loading stage. After that, the values of ratcheting strain of the two (BM and MAO) specimens gradually increase with the loading cycles. Correspondingly, the hysteresis loop evolves in a symmetric shape after the initial stage (Fig. 4a), indicating that dislocation slip dominates cyclic deformation. For the pre-corroded (BM and MAO) specimens, the values of ratcheting strain are basically constant and positive during the whole cyclic loading, which means that the cyclic deformation mechanism is dislocation slip. In addition, the absolute value of ratcheting strain in the non-corroded MAO specimen is higher than that in the non-corroded BM specimen, while the absolute value of ratcheting strain in the pre-corroded MAO specimen is lower than that in the pre-corroded BM specimen (Fig. 5a). In this case, the fatigue life of the non-corroded MAO specimen is lower than that of the non-corroded BM specimen, while the fatigue life of the pre-corroded MAO specimen is greater than that of the pre-corroded BM specimen. This shows that defects such as micro-pores and micro-cracks on the surface of the MAO coating reduce the fatigue life of material in the air environment, however, the MAO coating after pre-corroded can play a protective role on the substrate, and thus the corrosion fatigue resistance of the substrate is improved.

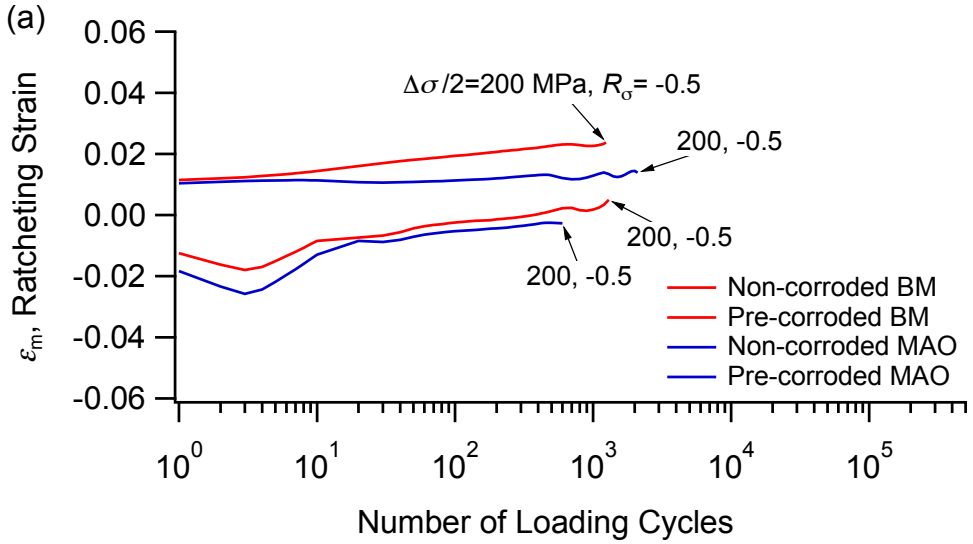

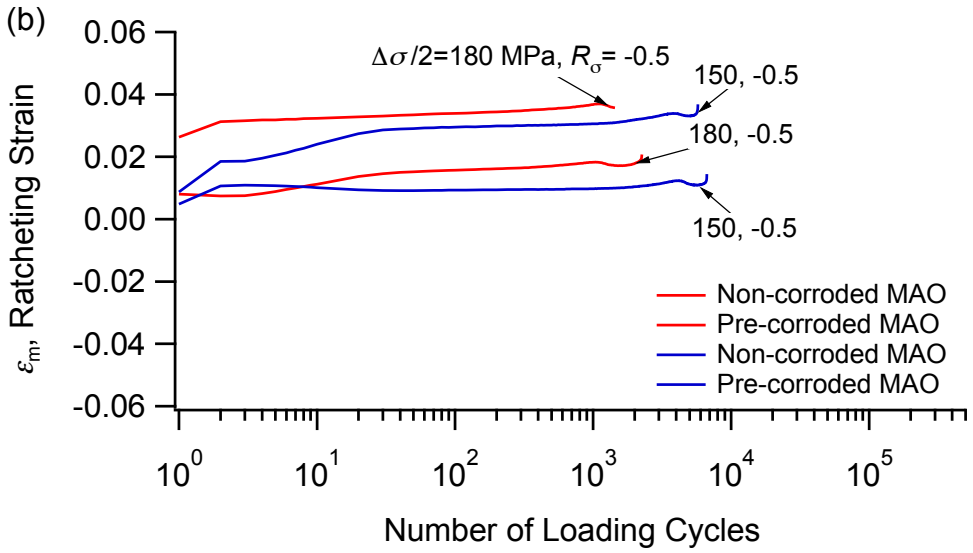

Fig. 5. Evolutions of ratcheting strain with cycle numbers at different stress amplitude with stress ratio of –0.5: (a) 200 MP and (b) 180 MPa and 150 MPa.

When the stress amplitude decreases to 180 MPa or 150 MPa (Fig. 5b), the value of ratcheting strain of the non-corroded specimen is positive and close to zero during the cyclic loading. At the same stress amplitude, the values of ratcheting strain in the pre-corroded MAO specimens are positive and higher than those in the non-corroded MAO specimens, and the fatigue lives of the pre-corroded specimens are lower than those of the non-corroded specimens. This may be due to the fact that the pre-corroded specimens are more vulnerable to fatigue failure under the interaction of corrosion and ratcheting strain.

3.3.2 Stress ratio of $R_\sigma = -0.8$

Fig. 6 shows the evolution of hysteresis loops of the two (BM and MAO) specimens under the different stress amplitudes with stress ratio of –0.8. When the stress amplitude is 200 MPa (Fig. 6a-d), the maximum stress and minimum stress in each cyclic loading are 223 MPa and -177 MPa, respectively. For the non-corroded BM specimens (Fig. 6a), the maximum compressive stress (177 MPa) is higher than monotonic compressive yield stress (159 MPa), while the maximum tensile stress (223 MPa) is much lower than the tensile yield stress (286 MPa). In this case, tension twinning activated in the compression reversal cannot be completely detwined in the subsequent tension reversal. This type of twinning-detwinning behavior is called as “partial twining- partial detwinning” [30]. Correspondingly, the compression reversal shows a concave-up shape, while the tension reversal exhibits a concave-down shape. In this case, the maximum strain and minimum strain of non-corroded specimens move along the negative direction with the cycle numbers increasing, showing the ratcheting strain accumulation in the negative direction. The evolution of hysteresis loops of the non-corroded MAO specimen (Fig. 6b) is similar to that of the non-corroded BM specimen, however, the maximum strain of the non-corroded MAO specimen moves in a negative direction while the values of minimum strain is almost constant. For the pre-corroded (BM and MAO) specimens (Fig. 6c and d), the cyclic stress-strain hysteresis loops show a sigmoidal shape in both compression and tension branches, indicating that the cyclic deformation mechanism is "complete twinning-complete detwinning". The results of previous studies [24] show that twinning under

compression has reached an exhaustion when the strain reaches –9.4%. Therefore, the pre-corroded specimen is completely twinned when the material is compressed to about –10%, and the subsequent plasticity deformation is dominated by dislocation slip. It is noted that the ϵ_{max} and ϵ_{min} of the pre-corroded specimens develop in the opposite direction, and the size of the hysteretic loops decreases gradually with the increase of loading cycles. In addition, the size of hysteresis loops of the pre-corroded specimens (Fig. 6c and d) is larger than that of the non-corroded specimens (Fig. 6a and b) at the same loading cycles.

For the stress amplitude of 180 MPa (Fig. 6e-h), the stress range is between 200 MPa and 160 MPa. The maximum compressive stress (160 MPa) of the non-corroded BM specimen (Fig. 6e) is close to the compressive yield stress (159 MPa), while the maximum tensile stress (200 MPa) is much lower than the tensile yield stress (286 MPa). In this case, the partial twins activated in the compression reversal are completely detwined in the subsequent tension reversal, and the stress-strain hysteresis loops show a concave-up shape in the compression reversal and a sigmoidal shape in the tension reversal, indicating that partial twinning-complete detwinning dominate cyclic deformation. Under this stress amplitude, the ϵ_{max} and ϵ_{min} in the non-corroded BM specimen move negatively with the increase of cycle number. The evolution of hysteresis loops and the accumulation of maximum/minimum strains in the MAO specimens are similar to that in the BM specimens. The size of the hysteretic loops in the non-corroded MAO specimens is larger than that in the non-corroded BM specimen, however, the size of the hysteretic loops in the pre-corroded MAO specimen is lower than that in the pre-corroded BM specimen.

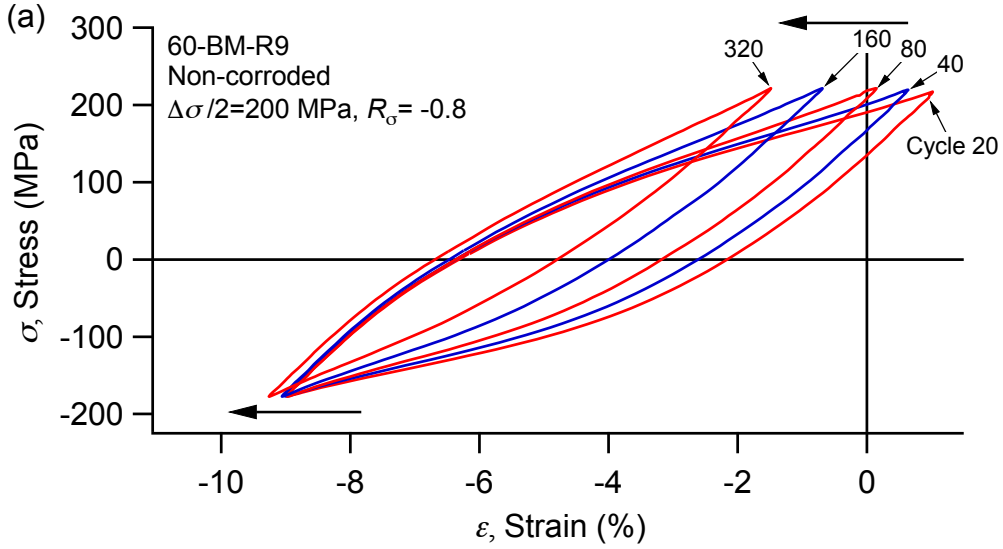

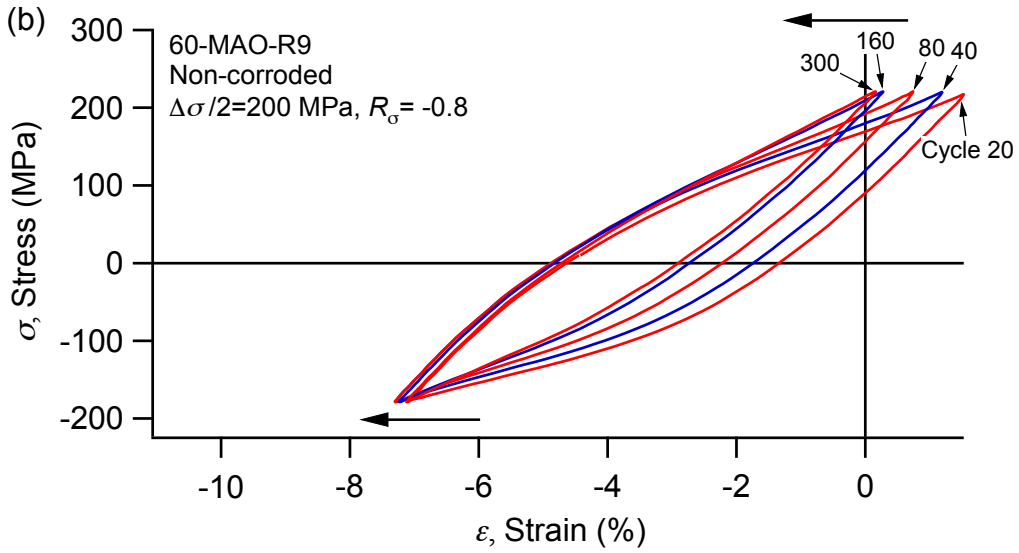
(b)
60-MAO-R9
Non-corroded
Δσ/2=200 MPa, Rσ= -0.8
300
160
80 40
Cycle 20
σ, Stress (MPa)
ε, Strain (%)

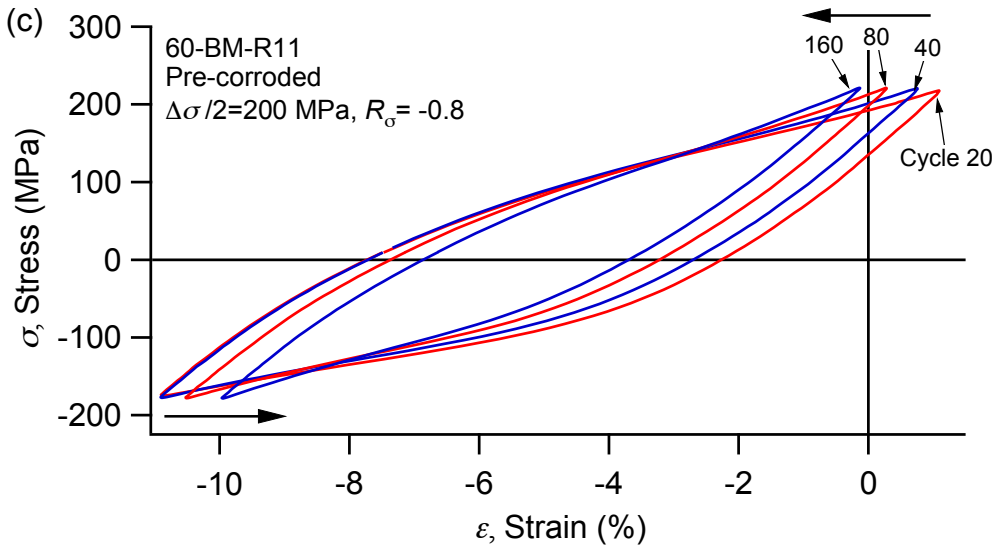
(c)
60-BM-R11
Pre-corroded
Δσ/2=200 MPa, Rσ= -0.8
160
80
40
Cycle 20
σ, Stress (MPa)
ε, Strain (%)

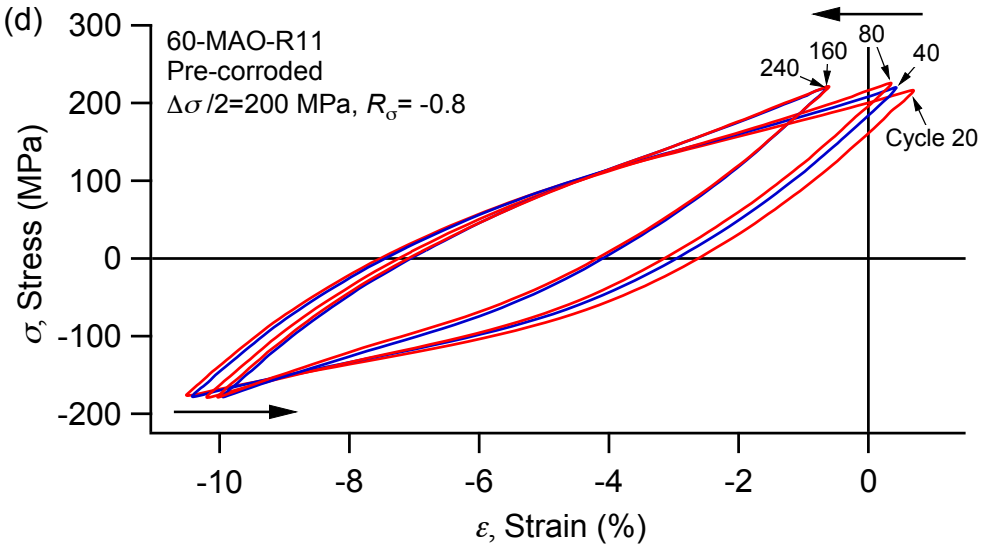
(d)
60-MAO-R11
Pre-corroded
Δσ/2=200 MPa, Rσ= -0.8
240
160
80
40
Cycle 20
σ, Stress (MPa)
ε, Strain (%)

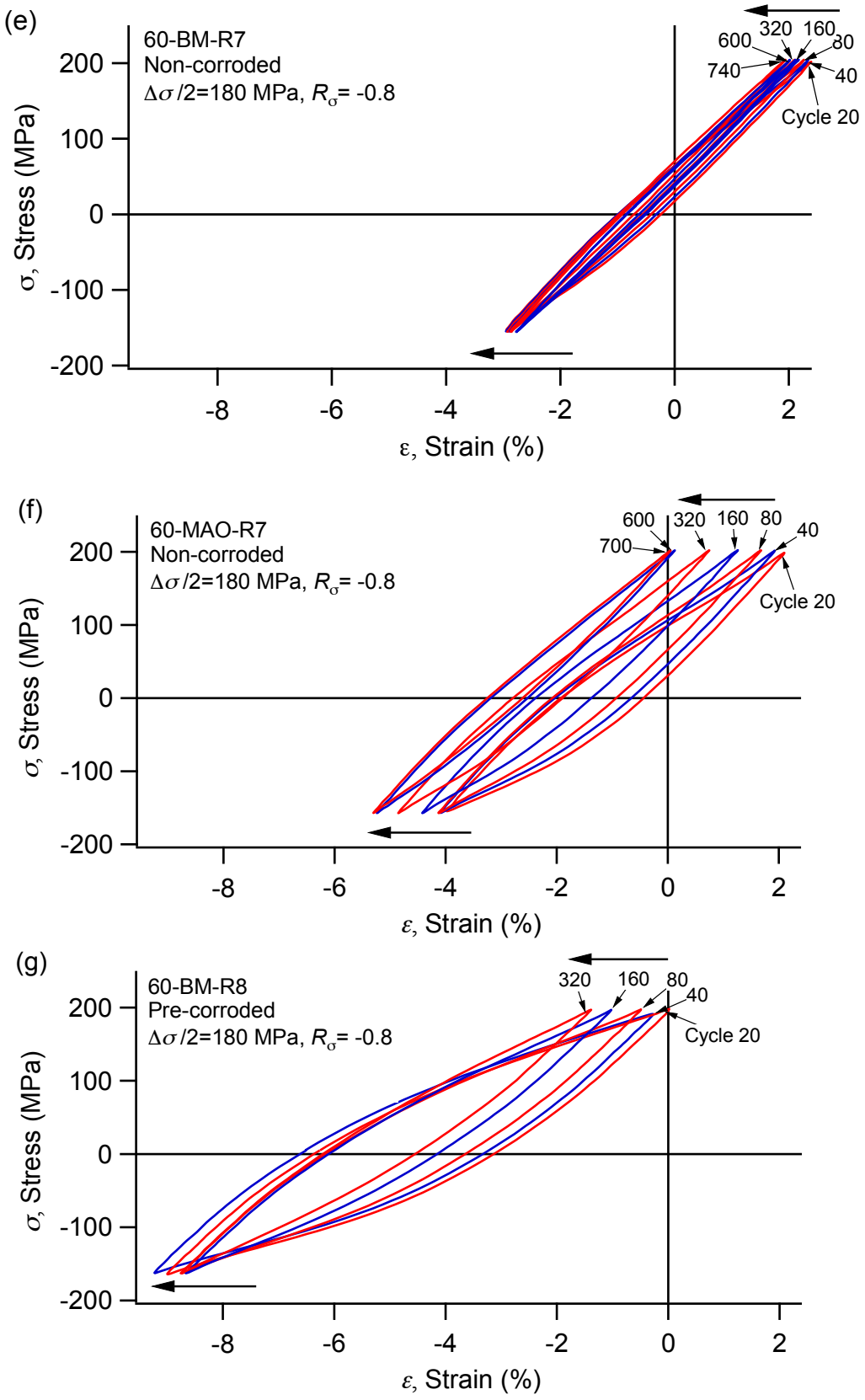
(e)
60-BM-R7
Non-corroded
Δσ/2=180 MPa, Rσ= -0.8
600
320
160
80
740
40
Cycle 20
σ, Stress (MPa)
ε, Strain (%)
(f)
60-MAO-R7
Non-corroded
Δσ/2=180 MPa, Rσ= -0.8
600
320
160
80
40
700
Cycle 20
σ, Stress (MPa)
ε, Strain (%)
(g)
60-BM-R8
Pre-corroded
Δσ/2=180 MPa, Rσ= -0.8
320
160
80
40
Cycle 20
σ, Stress (MPa)
ε, Strain (%)

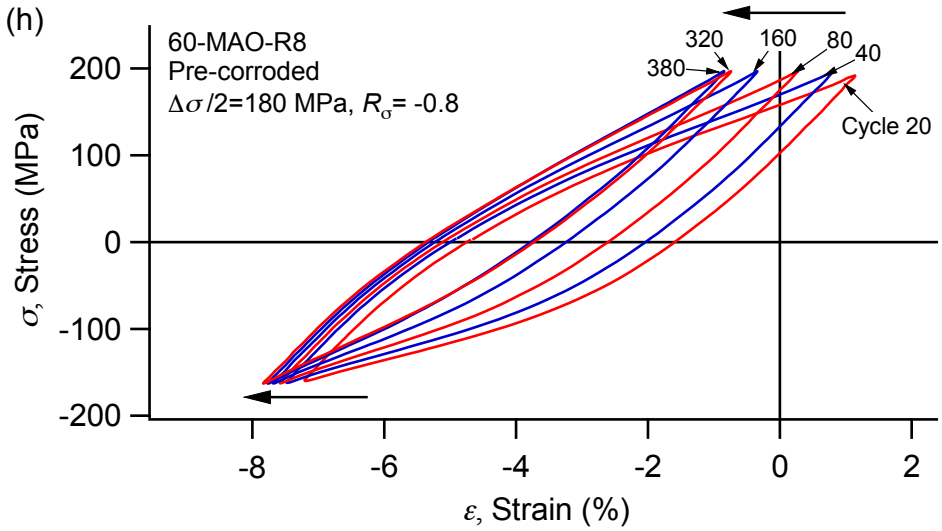

Fig. 6. Cyclic stress-strain hysteresis loops of specimens at stress ratio of –0.8: a) $\Delta\sigma/2$ = 200 Mpa, non-corroded BM; b) $\Delta\sigma/2$ = 200 Mpa, non-corroded MAO; c) $\Delta\sigma/2$ = 200 Mpa, pre-corroded BM; d) $\Delta\sigma/2$ = 200 Mpa, pre-corroded MAO; e) $\Delta\sigma/2$ = 180 Mpa, non-corroded BM; f) $\Delta\sigma/2$ = 180 Mpa, non-corroded MAO; g) $\Delta\sigma/2$ = 180 Mpa, pre-corroded BM and h) $\Delta\sigma/2$ = 180 Mpa, pre-corroded MAO.

The evolutions of ratcheting strain with cycle numbers under the different stress amplitudes with the stress ratio of –0.8 for all the specimens are shown in Fig. 7. At the stress amplitude of 200 MPa (Fig. 7a), the non-corroded and pre-corroded specimens show a compressed ratcheting strain. The ratcheting strain gradually decreases with the increase of loading cycle, and the drop degree of ratcheting strain of pre-corroded specimen is higher than that of non-corroded specimen. This is attributed to the cyclic deformation of the non-corroded specimen dominated by "partial twinning-partial detwinning", while the cyclic deformation of the pre-corroded specimen dominated by “complete twinning-complete detwinning”. The absolute value of ratcheting strain of the non-corroded specimen is lower than that of the pre-corroded specimen, and the fatigue life of the pre-corroded specimen is correspondingly lower than that of the non-corroded specimen. At the same environment, the fatigue life of the not-corroded MAO specimen with large absolute value of ratcheting strain is lower than that of the not-corroded BM specimen, and the fatigue life of the pre-corroded MAO specimen with smaller absolute value of ratcheting strain is higher than that of the pre-corroded BM specimen.

When the stress amplitude is 180 MPa (Fig. 7b), the values of ratcheting strain of the two specimens with non-corroded and pre-corroded are negative, and the ratcheting strain decreases with the increase of loading cycles. However, the drop degree of ratcheting strain of the pre-corroded specimen is similar to that of the non-corroded specimen. For the same specimen, the drop degree of ratcheting strain at the stress amplitude of 180 MPa is lower than that at the stress amplitude of 200 MPa. It may be related to the volume fraction of twins. The fraction volume of twins activated at lower stress amplitude is lower than that at higher stress amplitude [25]. In addition, it can be seen from Fig. 7 that the absolute value of ratcheting strain increases with the increase of stress amplitude. The correlation between the absolute value of ratcheting strain and the fatigue life is consistent with the result observed at the stress amplitude of 200 MPa.

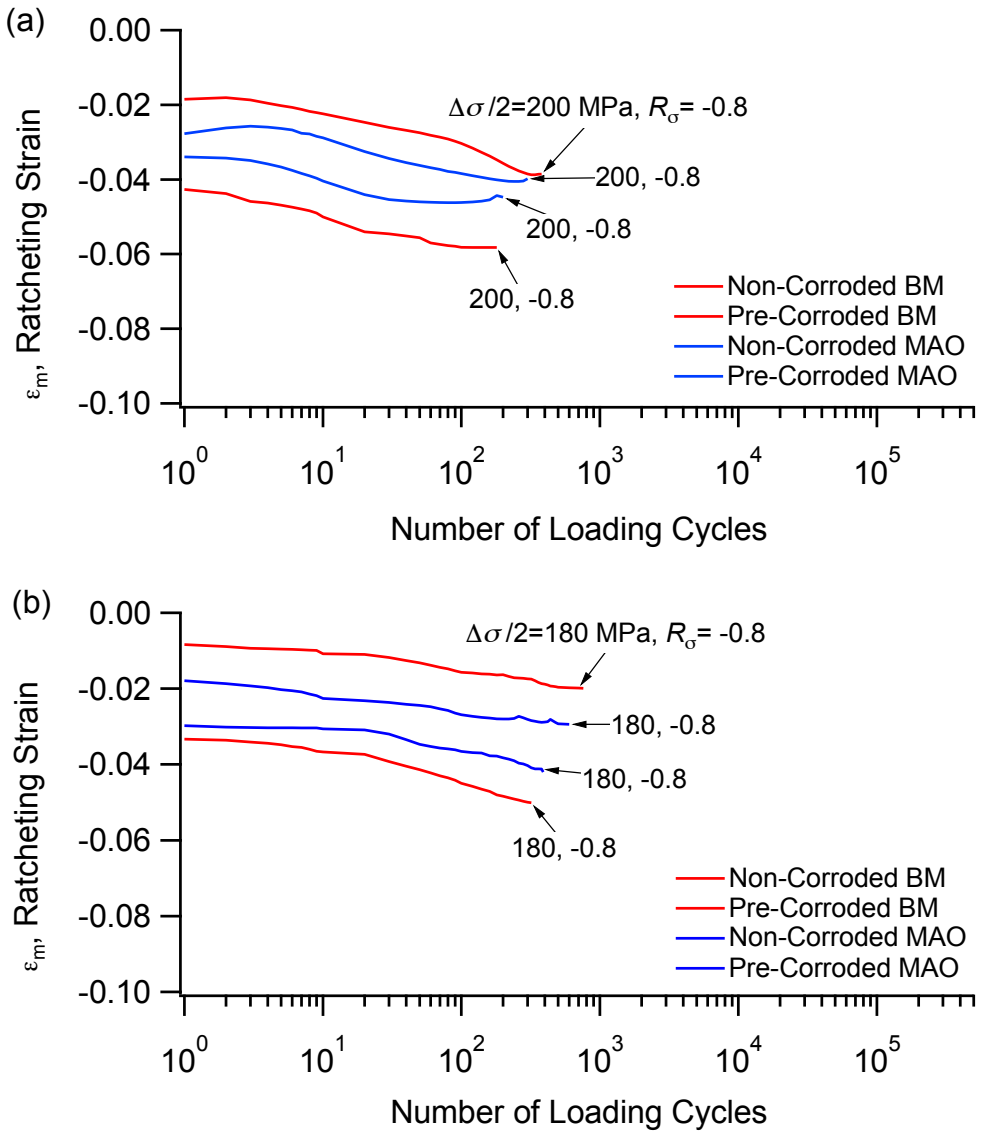

Fig. 7. Evolutions of ratcheting strain with cycle numbers at different stress amplitude with stress ratio of –0.8: (a) 200 MP and (b) 180 MPa.

3.3.3 Stress ratio of $R_\sigma = -1$

In general, the ratcheting effect occurs in the isotropic materials under asymmetric stress loading. However, ratcheting strain present in the anisotropic magnesium alloys even under symmetrical stress loading mode [31]. Fig. 8 represents the evolution of hysteresis loops of the different specimens at the symmetric stress-controlled loading. In the stress amplitude of 180 MPa (Fig. 8a-d), the shape of hysteresis loops always remains symmetrical and its size decreases gradually with the increase of loading cycles. The size of the hysteresis loop of the pre-corroded specimens is larger than that of the non-corroded specimens at the same loading cycles. Under the same stress amplitude of 180 MPa, the cyclic deformation behavior at the stress ratio of –1 is similar to that at the stress ratio of –0.8, and twinning-detwinning is involved in cyclic deformation. The ϵ_{max} andϵ_{min} of the BM specimen moves negatively simultaneously (Fig. 8a and c). However, the ϵ_{max} of the MAO specimen moves negatively while the ϵ_{min} is almost constant (Fig. 8b and d).

When the stress amplitude is 150 MPa (Fig. 8e and f), the range of cyclic stress of MAO specimen is between 150 MPa and -150 MPa. The stress level is not sufficient to activate the tension twinning, and the shape of hysteresis loops remains symmetrical during the cyclic loading, indicating that the cyclic plastic deformation is dominated by dislocation slip. However, the ϵ_{max} andϵ_{min} move in a negative direction with the increase of loading cycle, and the accumulation of ratcheting strain of the pre-corroded specimen is obvious compared to the non-corroded specimen. It is noted that although the cyclic deformation mechanism at the stress ratio of –1 is the same as that at the stress ratio of –0.5, their ratcheting strain behavior is different at the stress amplitude of 150 MPa.

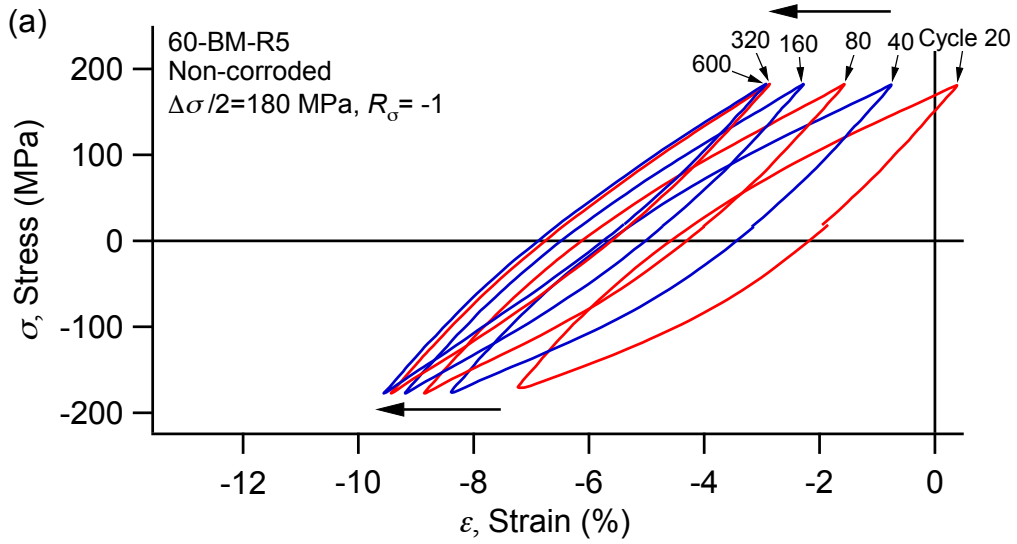

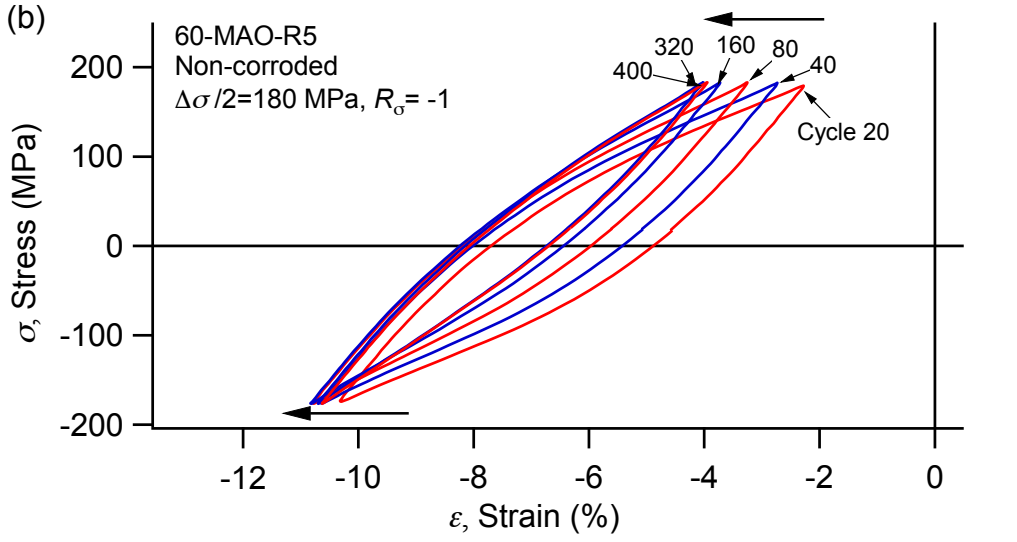

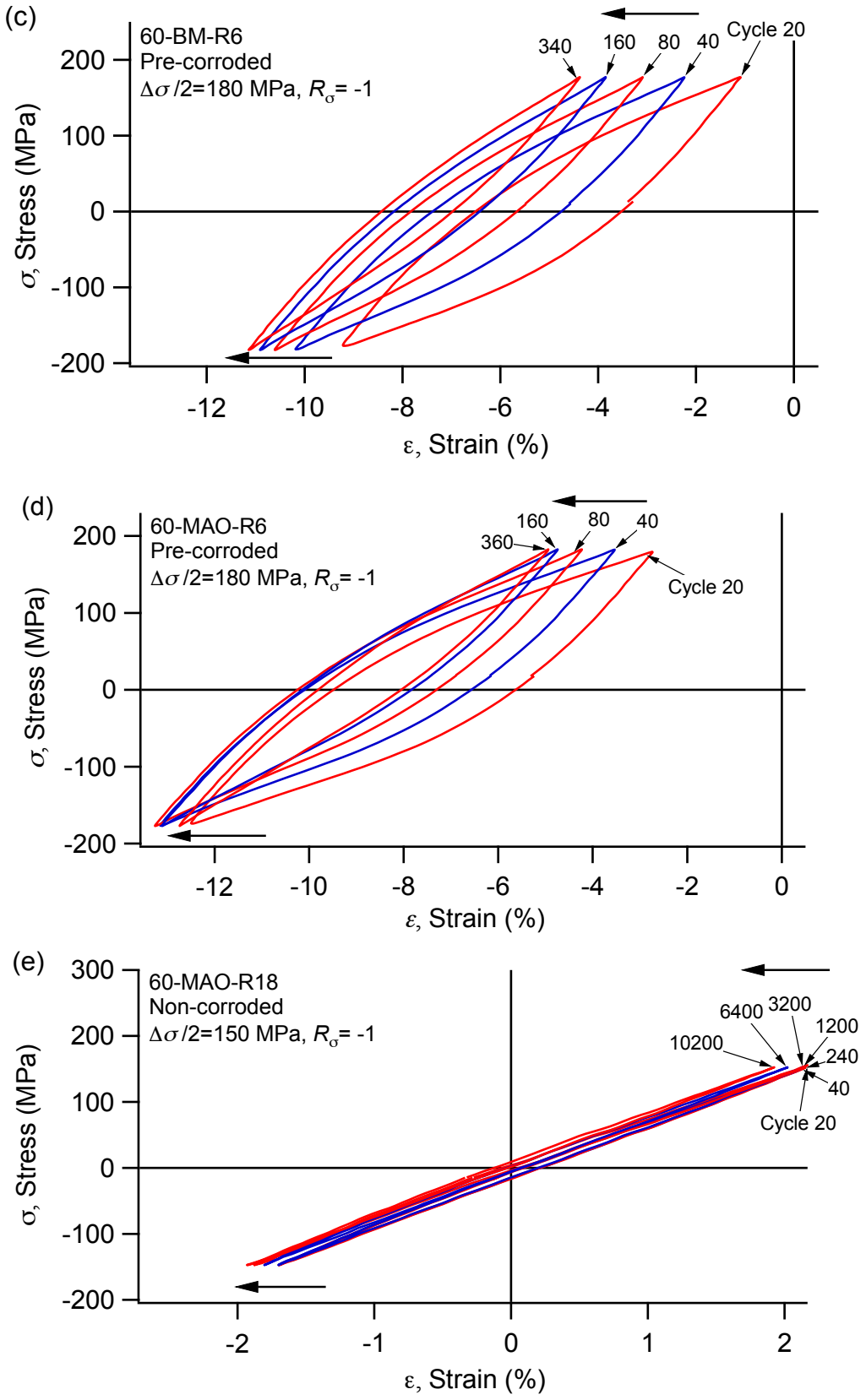
(c)
60-BM-R6
Pre-corroded
Δσ/2=180 MPa, R_σ= -1
340
160
80
40
Cycle 20
σ, Stress (MPa)
ε, Strain (%)
(d)
60-MAO-R6
Pre-corroded
Δσ/2=180 MPa, R_σ= -1
360
160
80
40
Cycle 20
σ, Stress (MPa)
ε, Strain (%)
(e)
60-MAO-R18
Non-corroded
Δσ/2=150 MPa, R_σ= -1
10200
6400
3200
1200
240
40
Cycle 20
σ, Stress (MPa)
ε, Strain (%)

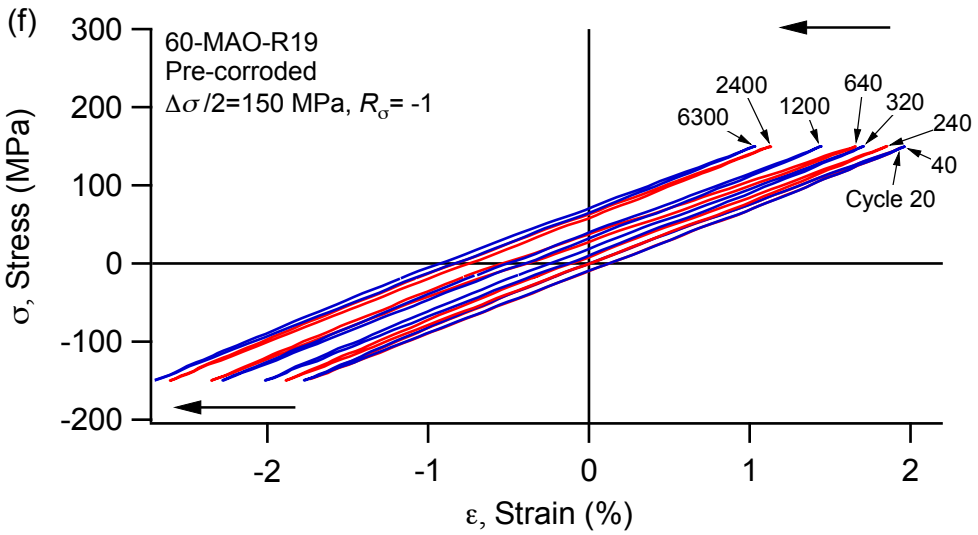

Fig. 8. Cyclic stress-strain hysteresis loops of specimens at stress ratio of –1: a) $\Delta\sigma/2$ = 180 Mpa, non-corroded BM; b) $\Delta\sigma/2$ = 180 Mpa, non-corroded MAO; c) $\Delta\sigma/2$ = 180 Mpa, pre-corroded BM; d) $\Delta\sigma/2$ = 180 Mpa, pre-corroded MAO; e) $\Delta\sigma/2$ = 150 Mpa, non-corroded MAO; f) $\Delta\sigma/2$ = 150 Mpa, pre-corroded MAO.

Fig. 9 shows the evolutions of ratcheting strain with cycle numbers under the different stress amplitudes with stress ratio of –1. At the stress amplitude of 180 MPa (Fig. 9a), the evolution of ratcheting strain of the pre-corroded (BM and MAO) specimens is similar to that of the non-corroded (BM and MAO) specimens. At the initial 10 cycles, the values of ratcheting strain decrease slowly with the loading cycles. After 10 cycles, the values of ratcheting strain decreases rapidly with the increase of cycle number. The ratcheting deformation behavior at the initial 10 cycles is related to the peak stress not reaching the set value. The difference of drop degree of ratcheting strain is related to the number of twinning-detwinning involved in deformation. When the stress amplitude is 150 MPa (Fig. 9b), the values of ratcheting strain of the non-corroded and pre-corroded MAO specimens remains stable during the cyclic loading, however, the strain value of the former is close to zero and the latter is negative. The absolute value of ratcheting strain of pre-corroded specimen is larger than that of non-corroded specimen, and the fatigue life of the latter is larger than that of the former for the same specimens. This indicates that the corrosion medium damages the integrity of the specimen surface, thus reducing the fatigue life of the specimen.

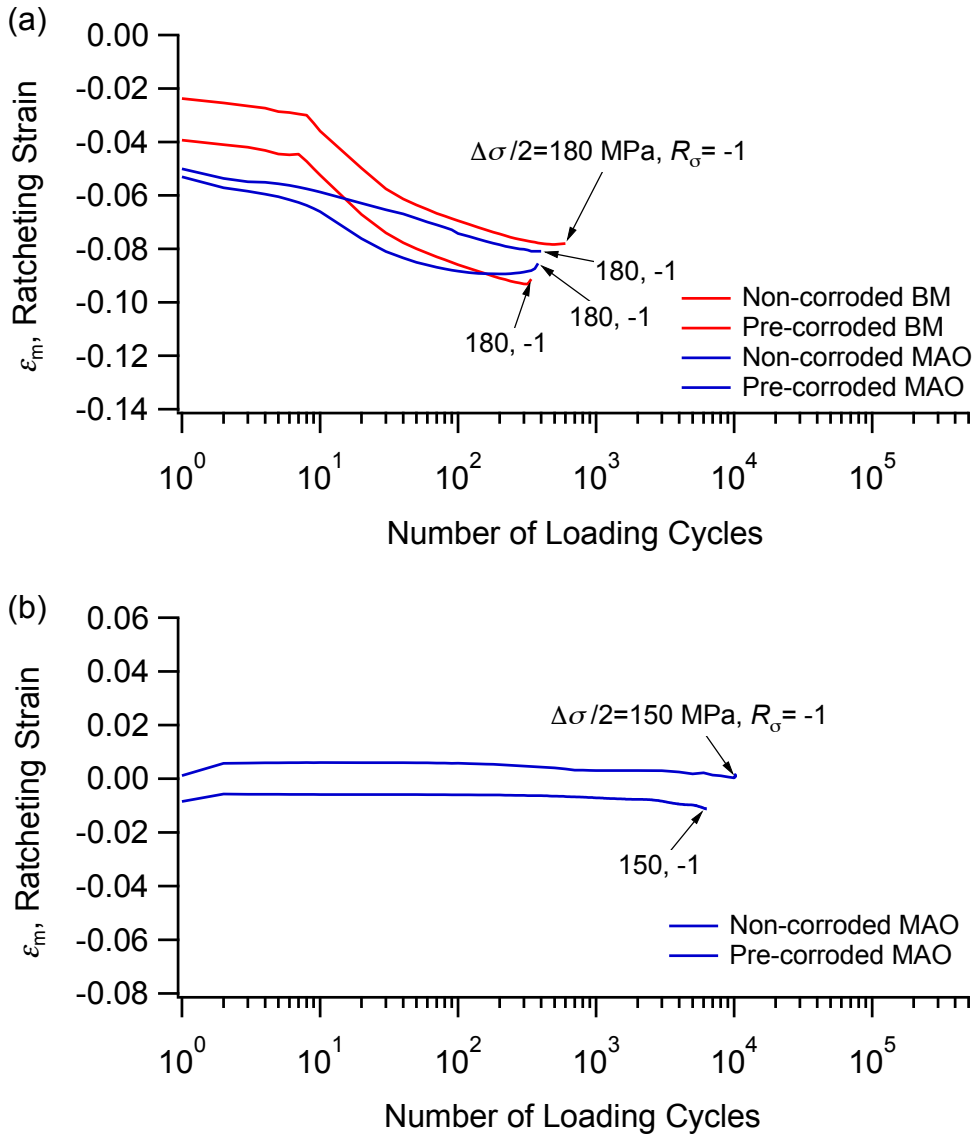

Fig. 9. Evolutions of ratcheting strain with cycle numbers at different stress amplitude with stress ratio of –1: (a) 180 MP and (b) 150 MPa.

3.4 Fatigue fracture morphologies

Fig. 10 shows SEM images observed on the fractured surface of specimens at the strain amplitude of 1% for the non-corroded and pre-corroded (BM and MAO) specimens. Region A represents the area of crack initiation and propagation. It can be seen that the number of crack initiation sites (white arrows) of the non-corroded specimens (Fig. 10a and b) is lower than that of the pre-corroded specimens (Fig. 10c and d), and the area of region A in the former is larger than that in the latter. The larger the region A, the slower the crack initiation and propagation rate, which indicates that the specimen has better fatigue resistance. The experimental results show that pre-corroded accelerates the initiation of crack, and the specimen is more vulnerable to fatigue failure. In addition, the number of crack initiation sites in the non-corroded BM specimens is less than that of the non-corroded MAO specimens, and the size of region A in the former is larger than that in the latter, whereas the situation of the pre-corroded specimens is the opposite. This indicates that MAO

coating can improve the fatigue life of AZ80 magnesium alloys in SBF. This is consistent with the results of fatigue life (Table 1).

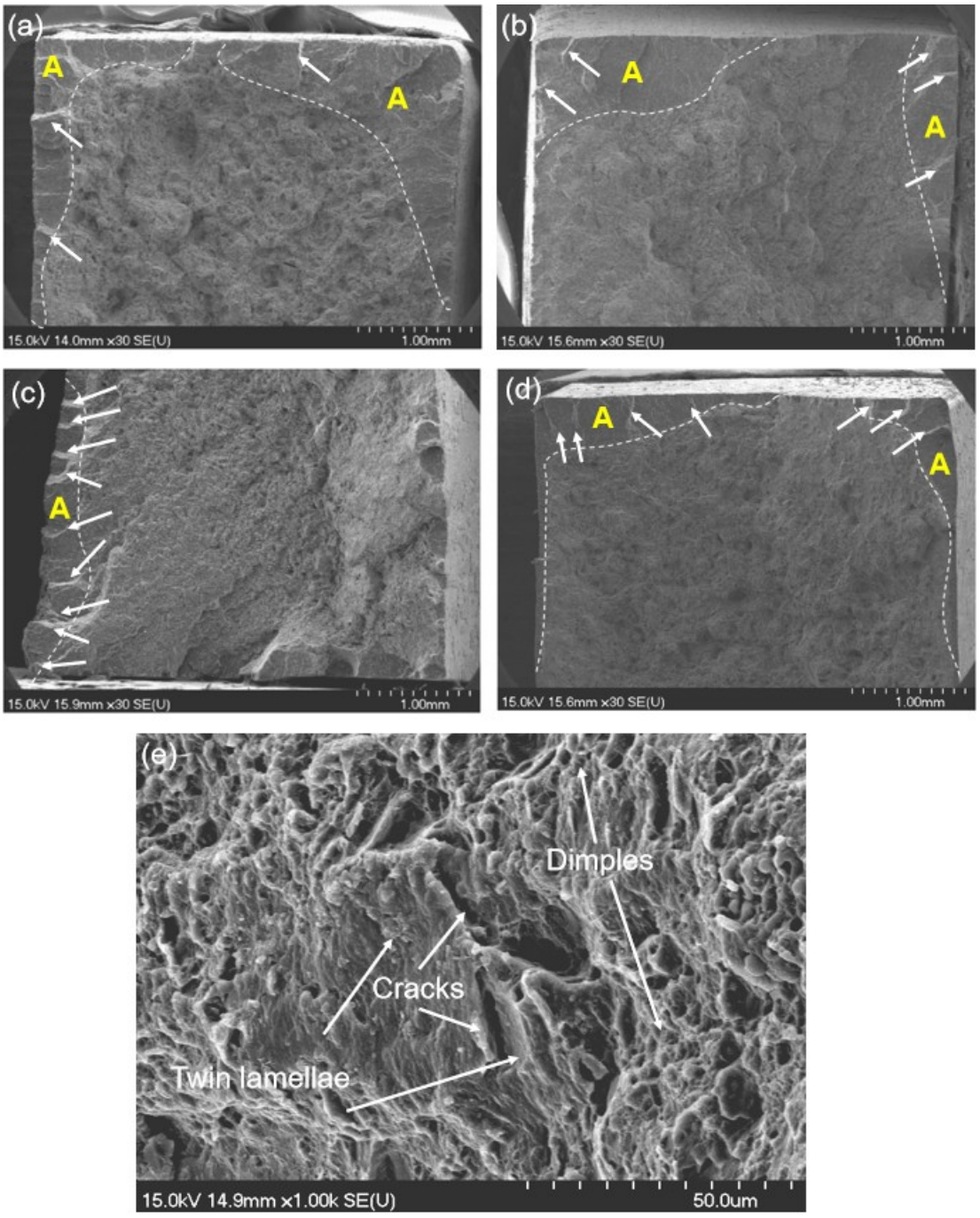

Fig. 10. SEM images of different specimens observed on fractured surface at strain amplitude of 1%: (a) non-corroded BM specimen; (b) non-corroded MAO specimen; (c) pre-corroded BM specimen; (d) pre-corroded MAO specimen; (e) High-magnified images taken in region B in figure (d).

The morphology of the crack propagation region of the BM and MAO specimens is similar at the same loading conditions. High-magnified images taken in the propagation region in Fig. 10d is shown in Fig. 10e. It is found that the region shows a mixed morphology composed of dimples and stripes. The fatigue stripes in magnesium alloys might be resulted from the twinning-detwinning

process in cyclic loading [32, 33]. In addition, some parallel secondary cracks associated with twinning can be observed in this region. This is consistent with the results observed in references [34, 35]. The above results confirm that the cyclic deformation mechanism is related to twinning-detwinning at the strain amplitude of 1%.

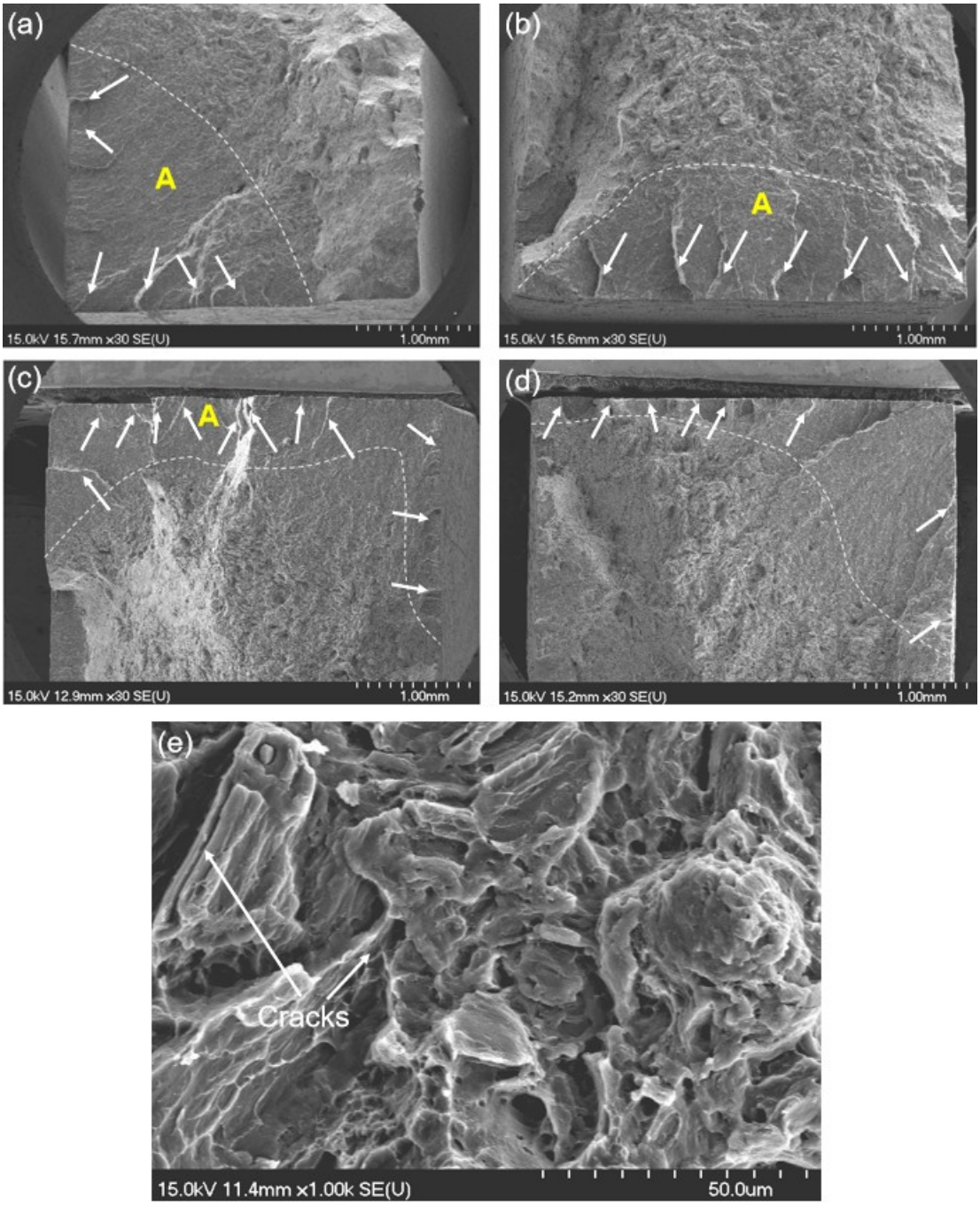

Fig. 11. SEM images of different specimens observed on fractured surface at stress amplitude of 200 MPa with stress ratio of -0.5: (a) non-corroded BM specimen; (b) non-corroded MAO specimen; (c) pre-corroded BM specimen; (d) pre-corroded MAO specimen; (e) High-magnified images taken in region B in figure (d).

Fig. 11 shows SEM images of the fractured surfaces at the stress amplitude of 200 MPa with a stress ratio of –0.5 for the BM and MAO specimens. The size of region A in the non-corroded BM specimen (Fig. 11a) is higher than that of non-corroded MAO specimen (Fig. 11b), and the number of crack initiation sites in the former is lower than that in the latter. Therefore, the fatigue life of the non-corroded MAO specimen is lower than that of the non-corroded BM specimen (Table 2). For the pre-corroded specimens, the size of region A in the MAO specimen (Fig. 11d) is larger than that of the BM specimen (Fig. 11c), and the number of crack initiation sites in the former is less than that in the latter. It indicates that MAO coating can block the corrosion solution into the substrate, thus improving the corrosion fatigue resistance of the material.

Fig. 11e shows high-magnified micrograph taken in the propagation region in Fig. 11d. It can be seen that cleavage facets with some micro-cracks are found in the propagation region. This indicates that dislocation slip dominates the cyclic deformation at the stress amplitude of 200 Mpa with stress ratio of –0.5.

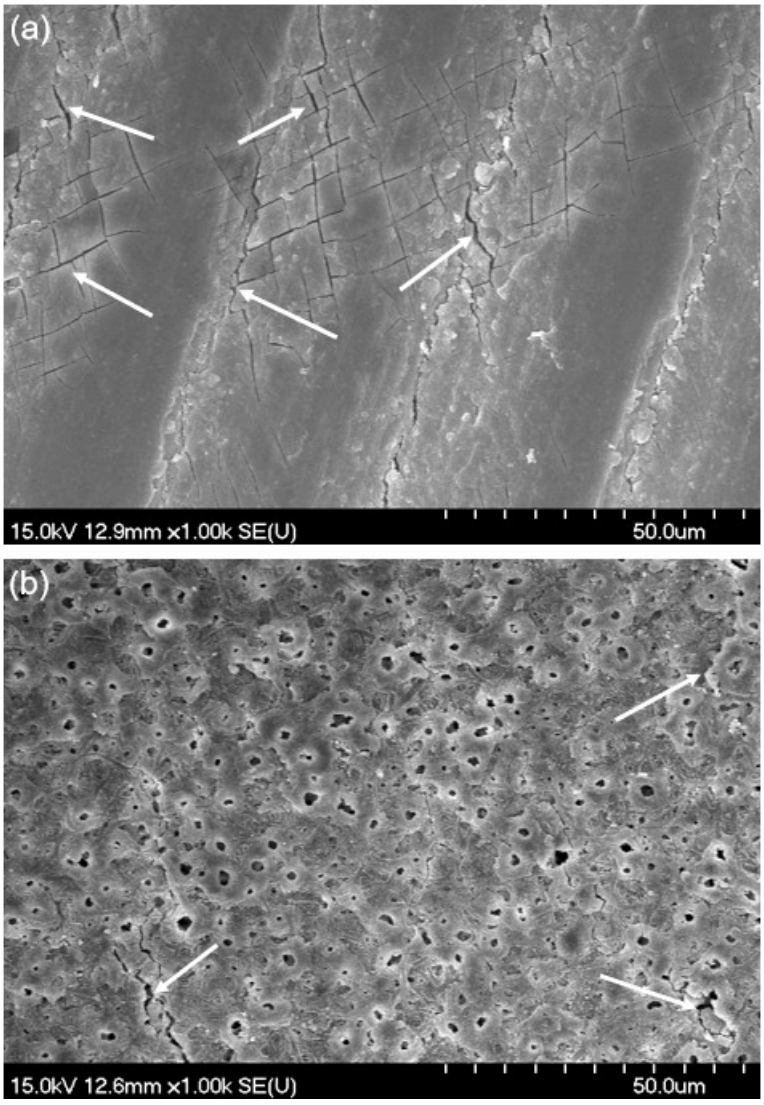

Fig. 12. Surface SEM images of pre-corroded specimens: (a) BM and (b) MAO.

Fig. 12 represents the surface SEM morphology of different pre-corroded specimens. As can be seen, there are more cracks (white arrows) on the surface of the pre-corroded BM specimen (Fig. 13a), which should correspond to the initiation sites of fatigue cracks. However, the number of cracks observed on the surface of the pre-corroded MAO specimen is significantly less than that of the pre-corroded BM specimen. It is noted that some corrosion products filled the micro-pores on the surface of the MAO coating, which improved the stress concentration caused by the micro-pores. Therefore, the number of crack initiation sites in the pre-corroded MAO specimens is lower than that in the pre-corroded BM specimens (see Figs. 10(c), 10(d), 11(c) and 11(d)).

3.5 Fatigue life

Generally, stress, strain, and energy-related terms are used as fatigue damage parameters to predict the fatigue life [36, 37]. One advantage of energy-based fatigue parameters is that the shape of hysteresis shape is considered and therefore suitable for predicting fatigue life of magnesium alloys [38]. Strain energy density is a parameter that contains the stress and strain of the material. The fatigue model using strain energy density as damage parameter can effectively explain the fatigue damage of materials under the different loading conditions [39]. Previous studies shown that strain energy density is a promising damage parameter to describe the fatigue life of magnesium alloys [40-47]. A total strain energy density is proposed as a damage parameter to predict fatigue life of materials, which is expressed as follows [43]:

$$\Delta W_t = \Delta W_p + \Delta W^{e+} \tag{1}$$

$$\Delta W^{e+} = \frac{\sigma_{\max}^2}{2E} \tag{2}$$

where ΔW_t, ΔW_p, ΔW^{e+}, σ_{max} and E are the total strain energy, plastic strain energy and positive elastic strain energy at half life cycle, and maximum stress and elastic modulus, respectively.

3.5.1 Fatigue model based on total strain energy density

The three-parameter equation method has been used by the author and co-authors to predict the fatigue life of many materials, and good prediction results have been obtained [44-47]. Therefore, the fatigue model established by using the total strain energy density as the damage parameter is as follows:

$$\left(\Delta W_t - FP_0\right)^m = C \tag{3}$$

where FP_0、m and C are fitting constants.

Fig. 13 is the result of fatigue life prediction based on total strain energy density. The fatigue test data of ZK60 magnesium alloys under strain-controlled loading and stress-controlled loading published by the author [25] are used to fit the constants in Equation 3, as shown in Fig. 13a. According to the fitted equation, the fatigue life is predicted by using the experimental data obtained in the reference [25] and the present paper, the results are shown in Fig. 13b. The black solid line indicates that the prediction results are consistent with the test results. The red dot lines are the factor-of-two (2×) boundaries, and the blue dotted lines are the factor-of-five (5×) boundaries. It can be seen that 98.8% of experimental data are included within a 2× scatter band, while 74.1% of the data within a 5× scatter band.

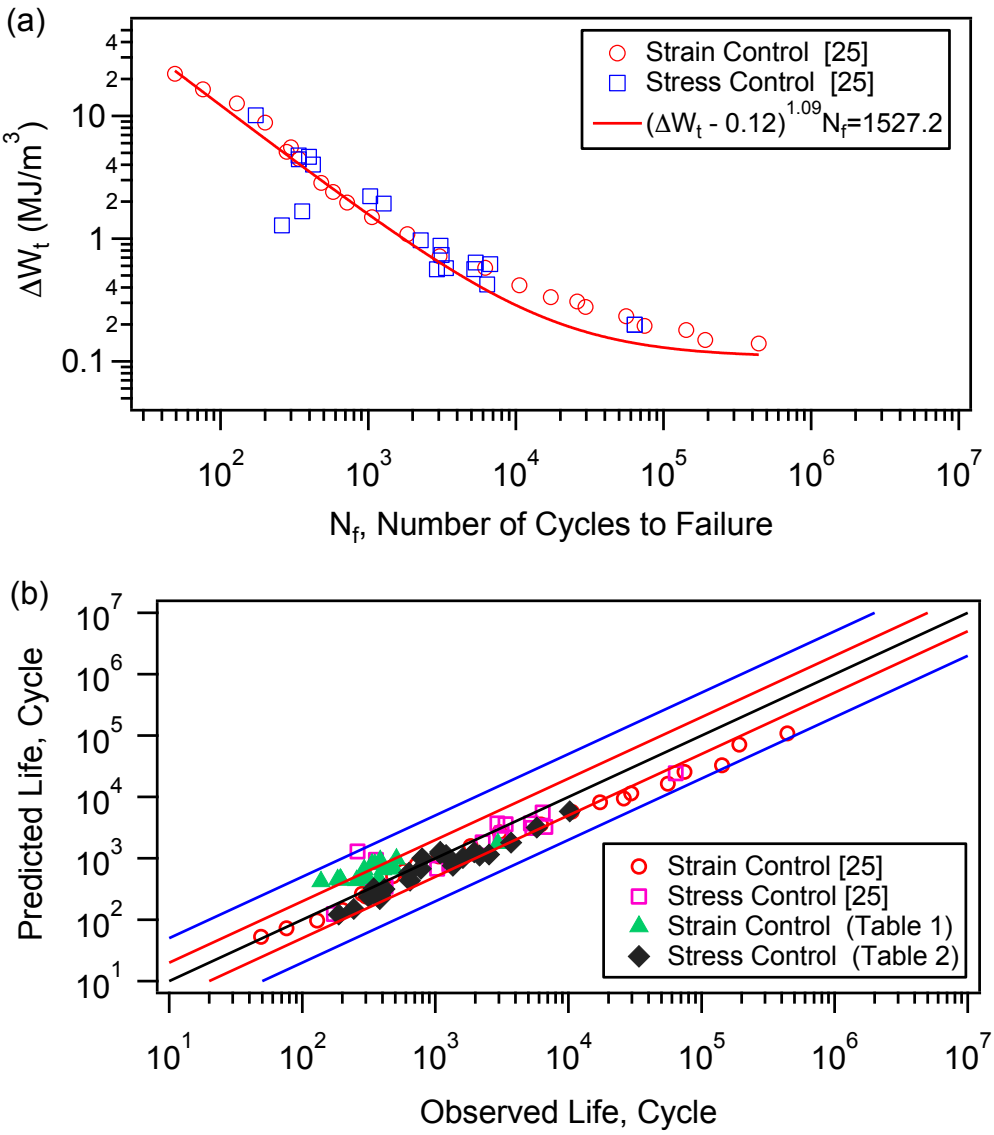

Fig. 13. Prediction results of fatigue life based on total strain energy: (a) relationship between total strain energy parameters and fatigue life; (b) relationship of predicted life and observed life.

3.5.2 Modified fatigue model based on total strain energy density

The results predicted by the total strain energy model are not very successful, which is attributed to the fact that the total strain energy model does not consider the asymmetric shape of the hysteresis loop of magnesium alloys during the cyclic loading. For this purpose, the negative elastic strain energy density is included in Equation 1, and the modified fatigue damage parameters are obtained by considering the weights of positive and negative elastic strain energy, as follows：

$$\Delta W_t^{'} = \Delta W_p + \Delta W^{em} \tag{4}$$

$$\Delta W^{em} = \eta \Delta W^{e+} + (1-\eta)\Delta W^{e-} \tag{5}$$

where ΔW_t^{*}, ΔW^{em}, ΔW^{e-*} and η are the modified total strain energy, modified elastic strain energy, negative elastic energy and Weighted factor. Equation 3 is used to fit the data in reference [25], and the results are shown in Fig. 14. It can be seen that all the predicted data are included within 5× scatter band, while 95.1% of the data within 2× scatter band. Compared with the total strain energy model, the prediction accuracy of the modified total strain energy model is improved by 21% in the 2× scatter band. Above results show that the modified total strain energy model can better predict the fatigue life and corrosion fatigue life of ZK60 magnesium alloys under different loading conditions.

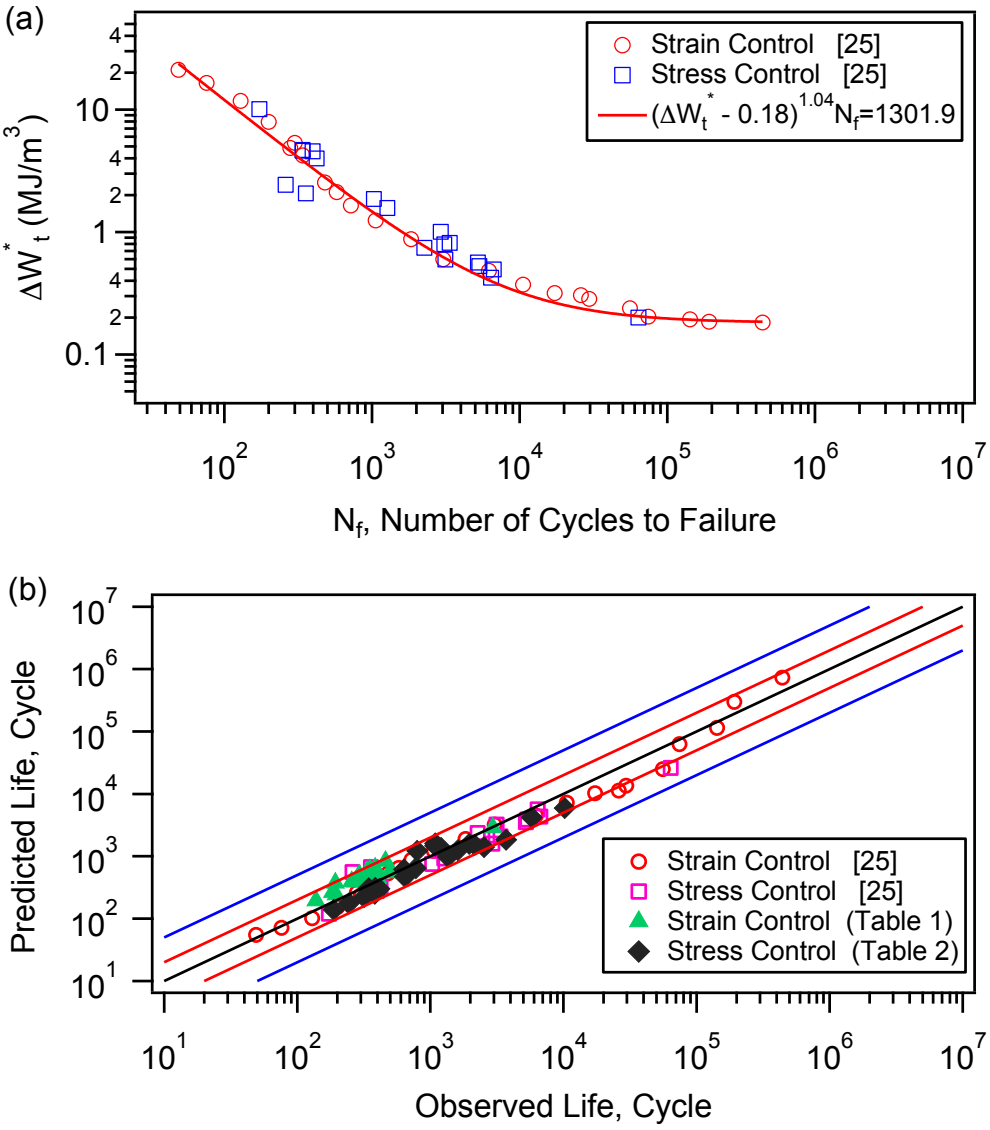

Fig. 14. Prediction results of fatigue life based on total strain energy: (a) relationship between modified total strain energy parameters and fatigue life; (b) relationship of predicted life and observed life.

4. Conclusions

MAO coating was prepared on the surface of ZK60 magnesium alloy. The substrate BM specimen and MAO treated specimen were pre-corroded in pH7.4 SBF for 12 h. The fatigue tests under different loading conditions were carried out for the specimens with non-corroded and re-

corroded, respectively. The following results are obtained.

(1) At the strain-controlled loading, the cyclic deformation of the non-corroded BM and non-corroded MAO specimens is dominated by twinning-detwinning at the strain amplitude of 0.7~1%, while dislocation slip dominates cyclic deformation at the strain amplitude of 0.5%. The cyclic deformation mechanism of the pre-corroded BM and pre-corroded MAO specimens is twinning-detwinning at the strain amplitude of 0.5~1%.

(2) At the stress-controlled loading, different cyclic deformation mechanisms based on stress amplitude and average stress, include partial twinning-complete detwinning, complete twinning-complete detwinning and partial twinning-partial detwinning. These deformation mechanisms have a great effect on ratcheting strain.

(3) At the same loading conditions, the absolute value of ratcheting strain in the pre-corroded MAO specimen is lower than that in the pre-corroded BM specimen, and the fatigue life of the former is greater than that of the latter, but the situation of the non-corroded specimen is the opposite.

(4) The modified total strain energy fatigue model can well predict the fatigue life of magnesium alloys under the different loading conditions.

Acknowledgements

The authors gratefully acknowledge the project sponsored by the support from National Natural Science Foundation of China (No. 51775502) and the Natural Science Foundation of Zhejiang Province (No. LY20E050024).

References

[1] Wittea F, Kaese V, Haferkamp H, Switzer E, Meyer-Lindenberg A, Wirth CJ, Windhagen H. In vivo corrosion of four magnesium alloys and the associated bone response. Biomaterials. 2005; 26: 3557-3563.

[2] Song YW, Shan DY, Chen RS, Zhang F, Han EH. Biodegradable behaviors of AZ31 magnesium alloy in simulated body fluid. Mater Sci Eng C. 2009; 29: 1039-1045.

[3] Gua YH, Chen CF, Bandopadhyay S, Ning CY, Zhang YJ, Guo YJ. Corrosion mechanism and model of pulsed DC microarc oxidation treated AZ31 alloy in simulated body fluid. Appl Surf Sci. 2012; 258: 6116-6126.

[4] Xu L, Pan F, Yu G. In vitro and in vivo evaluation of the surface bioactivity of a calcium phosphate coated magnesium alloy. Biomaterials. 2009; 30: 1512-1523.

[5] Tang H, Wu T, Wang H. Corrosion behavior of HA containing ceramic coated magnesium alloy in Hanks solution. J Alloys Compd. 2017; 698: 643-653.

[6] Guo XH, An MZ. Experimental study of electrochemical corrosion behaviour of bilayer on AZ31B Mg alloy. Corros Sci. 2010; 52: 4017-4027.

[7] Xu LP, Yu GN, Zhang E, Pan F, Yang K. In vivo corrosion behavior of Mg-Mn-Zn alloy for bone implant application. J Biomed Mater Res A. 2010; 3: 703-711.

[8] Yun YH, Dong ZY, Yang D, Schulz MJ, Shanov VN, Yarmolenko S, Xu ZY, Kumta P, Sfeir C. Biodegradable Mg corrosion and osteoblast cell culture studies. Mater Sci Eng C. 2009; 29: 1814-1821.

[9] Zhao QM, Li GZ, Zhu HM. Preparation and performance characterization of bioactive coating on magnesium Alloy. J Biobased Mater Bio. 2017; 11: 473-476.

[10] Wang ZX, Chen GQ, Chen LY, Xu L, Lu S. Degradation behavior of micro-arc oxidized ZK60

magnesium alloy in a simulated body fluid. Metals. 2018; 8: 724-741.
[11] Lin X, Tan LL, Zhang Q, Yang k, Hu ZQ, Qiu JH, Cai Y. The in vitro degradation process and biocompatibility of a ZK60 magnesium alloy with a forsterite-containing micro-arc oxidation coating, Acta. Biomaterials. 2013; 9: 8631-8642.
[12] Xiong Y, Lu C, Wang C, Song RG. Characterization and electrochemical corrosion behavior of biological ceramic coatings on alloy by micro-arc oxidation, J Biobased Mater Bio. 2014; 8: 158-164.
[13] Dou JH, Yu HJ, Chen CZ, Ma RLW, Yuen MMF. Preparation and microstructure of MAO/CS composite coatings on Mg alloy. Maters Lett. 2020; 271: 127729.
[14] Rojaeea R, Fathi M, Raeissi K. Electrophoretic deposition of nanostructured hydroxyapatite coating on AZ91 magnesium alloy implants with different surface treatments. Appl Surf Sci. 2013; 285P: 664-673.
[15] Xiong Y, Lu C, Wang C, Song RG. Degradation behavior of n-MAO/EPD bio-ceramic composite coatings on magnesium alloy in simulated body fluid. J Alloys Compd. 2015; 625: 258-265.
[16] Xiong Y, Shen YS, He LY, Yang ZY, Song RG. Stress corrosion cracking behavior of LSP/MAO treated magnesium alloy during SSRT in a simulated body fluid. J Alloys Compd. 2020; 822: 153707.
[17] Xiong Y, Hu Q, Song RG, Hu XX. LSP/MAO composite bio-coating on AZ80 magnesium alloy for biomedical application. Mater Sci Eng C. 2017; 75: 1299-1304.
[18] Chen LX, Sheng YY, Zhou HY, Lia ZB, Wang XJ, Li W. Influence of a MAO plus PLGA coating on biocorrosion and stress corrosion cracking behavior of a magnesium alloy in a physiological environment. Corros Sci. 2019; 148: 134-143.
[19] Singh Raman RK, Jafari S, Harandi SE. Corrosion fatigue fracture of magnesium alloys in bioimplant applications: A review. Eng Fract Mech. 2015; 137: 97-108.
[20] Jafari S, Raman RK, Davies HJ. Corrosion fatigue of a magnesium alloy in modified simulated body fluid. Eng Fract Mech. 2015; 137: 2-11.
[21] Liu MY, Wang J f, Zhu SJ, Zhang YB, Sun YF, Wang LG, Guan SK. Corrosion fatigue of the extruded Mg-Zn-Y-Nd alloy in simulated body fluid. J Alloys Compd. 2020; 8: 231-240.
[22] Chen G, Lu LT, Cui Y, Xing R, Gao H, Chen X. Ratcheting and low-cycle fatigue characterizations of extruded AZ31B Mg alloy with and without corrosive environment. Int J Fatigue. 2015; 80: 364-371.
[23] Xiong Y, Hu Q, Hu XX, Song RG. Microstructure and corrosion resistance of Ti_3O_5-HA bio-ceramic coating fabricated on AZ80 magnesium alloy. Surf Coat Technol. 2017; 325: 239-247.
[24] Xiong Y, Yu Q, Jiang YY. An experimental study of cyclic plastic deformation of extruded ZK60 magnesium alloy under uniaxial loading at room temperature. Int J Plast. 2014; 53: 107-124.
[25] Xiong Y, Yu Q, Jiang Y. Fatigue of ZK60 magnesium alloy under uniaxial loading. Int J Fatigue. 2014; 64: 74-83.
[26] Chen YL, Zhang Y, Li Y, Zhang TF. Influences of micro-arc oxidation on pre-corroded fatigue property of magnesium Alloy AZ91D. Advanced Materials Research. 2010; 152-153: 51-57.
[27] He XL, Wei YH, Hou LF, Yan ZF, Guo CL, Han PJ. Investigation on corrosion fatigue property of epoxy coated AZ31 magnesium alloy in sodium sulfate solution. Theor Appl Fract Mec. 2014; 70: 39-48.
[28] Shahzad M, Chaussumier M, Chieragatti R, Mabru C, Rezai-Aria F. Effect of sealed anodic film

on fatigue performance of 2214-T6 aluminum alloy. Surf Coat Technol. 2012; 206: 2733-2739.
[29] Yu Q, Zhang JX, Jiang YY. Direct observation of twinning–detwinning–retwinning onmagnesium single crystal subjected to strain-controlled cyclictension–compression in [0001] direction. Phil Mag Lett. 2011; 91: 757-765.
[30] Xiong Y, Yu Q, Jiang YY. Cyclic deformation and fatigue of extruded AZ31B magnesium alloy under different strain ratios. Mater Sci Eng A. 2016; 649: 93-103.
[31] Lin YC, Liu ZH, Chen MX, Chen J. Uniaxial ratcheting and fatigue failure behaviors of hot-rolled AZ31B magnesium alloy under asymmetrical cyclic stress-controlled loadings. Mater Sci Eng A. 2013; 573: 234-244.
[32] Lin XZ, Chen DL. Strain controlled cyclic deformation behavior of an extruded magnesium alloy. Mater Sci Eng A. 2008; 496: 106-113.
[33] Begum S, Chen DL, Xu S, Luo AA. Strain-controlled low-cycle fatigue properties of a newly developed extruded magnesium alloy. Metall Mater Trans A. 2009; 40: 255-255.
[34] Xiong Y, Jiang YY. Cyclic deformation and fatigue of rolled AZ80 magnesium alloy along different material orientations. Mater Sci Eng A. 2016; 677: 58-67.
[35] Toscano D, Shaha SK, Behravesh B, Jahed H, Williams B. Effect of forging on the low cycle fatigue behavior of cast AZ31B alloy. Mater Sci Eng A. 2017; 706: 342-356.
[36] Albinmousa J, Jahed H. Multiaxial effects on LCF behaviour and fatigue failure of AZ31B magnesium extrusion. Int J Fatigue. 2014; 67: 103-116.
[37] Kalatehmollaei E, Mahmoudi-Asl H, Jahed H. An asymmetric elastic–plastic analysis of the load-controlled rotating bending test and its application in the fatigue life estimation of wrought magnesium AZ31B. Int J Fatigue. 2014; 64: 33-41.
[38] Dallmeier J, Huber O, Saage H, Eigenfeld K. Uniaxial cyclic deformation and fatigue behavior of AM50 magnesium alloy sheet metals under symmetric and asymmetric loadings. Mater Des. 2015; 70: 10–30.
[39] Pahlevanpoura AH, Behravesha SB, Adibnazarib S, Jaheda H. Characterization of anisotropic behaviour of ZK60 extrusion under stresscontrol condition and notes on fatigue modeling. Int J Fatigue. 2019; 127: 101-109.
[40] Roostaei AA, Jahed H. Role of loading direction on cyclic behaviour characteristics of AM30 extrusion and its fatigue damage modeling. Mater Sci Eng A. 2016; 670: 26-40.
[41] Park SH, Hong SG, Yoon JH, Lee CS. Influence of loading direction on the anisotropic fatigue properties of rolled magnesium alloy. Int J Fatigue. 2016; 87: 210-215.
[42] Toscanoa D, Shaha SK, Behravesh B, Jahed H, Williams B. Effect of forging on the low cycle fatigue behavior of cast AZ31B alloy. Mater Sci Eng A. 2017; 706: 342-356.
[43] Ellyin F, Xia Z. A general fatigue theory and its application to out-of-phase cyclic loading. J Eng Mater Technol. 1993; 115: 411-416.
[44] Castro F, Jiang YY. Fatigue life and early cracking predictions of extruded AZ31B magnesium alloy using critical plane approaches. Int J Fatigue. 2016; 88: 236-246.
[45] Yu Q, Zhang JX., Jiang YY, Li QZ. Multiaxial fatigue of extruded AZ61A magnesium alloy, Int J Fatigue. 2011; 33: 437-447.
[46] Xiong Y, Yu Q, Jiang YY. Multiaxial fatigue of extruded AZ31B magnesium alloy. Mater Sci Eng A. 2012; 546: 119-128.
[47] Xiong Y, Jiang YY. Cyclic deformation and fatigue of rolled AZ80 magnesium alloy along different material orientations. Mater Sci Eng A. 2016; 677: 58-67.